Nonlinear control of the minimum safety factor in tokamaks by optimal allocation of spatially moving electron cyclotron current drive

Sai Tej Paruchuri [a,*], Andres Pajares [b], Tariq Rafiq [a], Eugenio Schuster [a]

[a] Mechanical Engineering and Mechanics, Lehigh University, Bethlehem, PA, USA
[b] General Atomics, San Diego, CA, USA

A B S T R A C T

The minimum value of the safety factor profile is related to the magnetohydrodynamic (MHD) stability of the plasma confined in a tokamak. Therefore, active control of the minimum safety factor may mitigate MHD instabilities that can degrade or even terminate plasma confinement. Typically, in most tokamak scenarios, the minimum safety factor evolves spatially with time, i.e., the location at which the safety factor achieves the minimum value changes with time. In addition to the inherent nonlinearities in the minimum safety factor evolution, its spatial variation makes the control design challenging. In particular, complexity in control design may arise from the need for time-dependent nonlinear models that account for spatial variation of the minimum safety factor. Furthermore, the minimum safety factor may drift to locations where the actuator authority is low. The problem of minimum safety factor control with target location tracking and moving electron cyclotron current drive (ECCD) is addressed in this work. A nonlinear time-dependent model that incorporates the spatial variation of the minimum safety factor is presented. A nonlinear controller based on optimal feedback linearization is developed to track a target minimum safety factor. The proposed controller treats the ECCD position as a controllable variable. In other words, the controller prescribes the ECCD position (in addition to the non-inductive powers) in real time based on an optimal criterion that is defined a priori. This work also presents the steps necessary to integrate the minimum safety factor controller with a total energy controller to achieve multiple control objectives simultaneously. The proposed integrated control algorithm is tested using nonlinear simulations in the Control Oriented Transport SIMulator (COTSIM) for a DIII-D tokamak scenario.

1. Introduction

Safety factor (q) profile regulation is critical for the operation of next-generation tokamaks like ITER. Well-established magnetohydrodynamic studies have linked the onset of MHD instabilities to the safety factor profile [1]. For instance, neoclassical tearing modes (NTMs) can appear at locations where the safety factor profile takes a rational value. Depending on the control objective, safety factor profile regulation can be broadly classified into (i) global safety factor regulation and (ii) local safety factor regulation. In global regulation, the objective is to control the entire safety factor profile, usually by driving to zero the difference or error between target and actual profiles [2]. This difference is usually quantified by the L_2 norm of the error profile (or equivalently by the sum of squared error) [3,4]. In local regulation, the objective is to control only on a limited section of the safety factor profile instead of the entire profile. Examples of local regulation include the control of the central safety factor q_0 [5,6] and q_{95} [7]. Tokamaks like ITER may require a combination of "coarse" global

control with "fine" local control to achieve stable, high-confinement, advanced scenarios.

Existing literature has multiple solutions for both global and local safety factor regulation. Both non-model-based [8–10] and model-based [5,6,11] proportional–integral–derivative (PID) controllers are among the most commonly implemented control algorithms. Furthermore, researchers have developed optimal feedback control algorithms, including the linear quadratic regulator and linear–quadratic integral controller [3,5,12,13]. Linear model predictive controllers have also been developed for safety factor profile control [7,14–16]. The above-cited literature relies on the "approximate and then control" approach, i.e., the partial differential equation is first discretized, and then a controller is designed. On the other hand, researchers in [17–19] implemented the "design a controller and then approximate" approach, however, with some simplifying assumptions. In this approach, the authors first developed an infinite-dimensional controller and then discretized the controller for practical implementation. Other controllers that have

* Corresponding author.
  E-mail address: saitejp@lehigh.edu (S.T. Paruchuri).

been developed for safety factor regulation include techniques such as feedback linearization [2,20–22], passivity-based control [23], backstepping control [24], H_∞ control [25], and reinforcement-learning-based control [26].

The minimum safety factor q_{min} is a property that is critical to plasma's MHD stability. In particular, maintaining the minimum safety factor above $q = 1$ could prevent sawtooth instability. Furthermore, advanced scenarios characterized by a high bootstrap current fraction could benefit from high q_{min} [27]. In addition, instabilities like NTMs could appear at locations with rational safety factor values. Maintaining the minimum safety factor above $q = 1.5$ or $q = 2$ could prevent the onset of NTMs. In each of these instances, the active regulation of the minimum safety factor becomes imperative, necessitating the development of a control algorithm that is implementable in the plasma control system (PCS). It is important to note that the minimum safety factor evolves spatially with time in most tokamak scenarios characterized by a reverse magnetic shear configuration. The spatial drift of the minimum safety factor over time can pose two challenges to control design. First, controllers synthesized based on models discretized on a fixed grid may not be efficient enough since these models do not capture the spatial evolution of q_{min}. In other words, the q_{min} cannot be associated with a particular point of the grid as it spatially drifts over time. Second, the location of q_{min} may drift to regions with low current depositions in some tokamak scenarios, particularly during the formation phase of the discharge, since the current depositions of the noninductive current drives used for control are not uniform across the whole spatial range, from the magnetic axis to the plasma boundary. This may impact the controllability of q_{min} as it moves to regions without much actuation capability. As a result, the controller can place high power demands on the noninductive drives to account for the low current deposition at the location of q_{min}. One can potentially solve this issue by allocating more noninductive drives to more uniformly cover the whole spatial range. However, next-generation tokamaks will have multiple control objectives. As a result, assigning more actuators for a specific control objective (the control of the minimum safety factor in this case) may not be optimal, or even possible.

Thus, the majority of control algorithms referenced above cannot be used to directly regulate q_{min}, as they focus on control of the safety-factor profile at fixed spatial points or integrated over the whole spatial domain. On the other hand, while Refs. [8,10,26] address the regulation of q_{min}, they do not provide a generic control solution for tracking a specified q_{min} target across different tokamak scenarios. The control strategy in these cases is based either on raising the whole profile above a desired value or on assuming a monotonic safety-factor profile, where the problem of controlling the minimum safety factor reduces to the much simpler problem of controlling the central safety factor (fixed spatial location). Ref. [9] introduces a notable model-free solution for q_{min} control, where the q_{min} value is calculated as the lowest q value across a predefined set of spatial locations. The controller in [9] then adjusts the feedback input based on the integral of the deviation between the computed q_{min} and the target. However, this approach does not address the controllability challenges related to the spatial drift of the minimum safety factor. It is also important to emphasize that a model-based approach could provide substantial benefits, particularly in terms of analyzing the stability, performance, and robustness of the closed-loop system. The controller described in [20] adopts a model-based approach for q_{min} regulation but relies on real-time optimization algorithms and similarly overlooks the controllability issues associated with q_{min}.

This work extends the preliminary studies presented in [20,21] and addresses the problem of regulating the spatially-drifting minimum safety factor while considering concurrent control objectives. In particular, the problem is addressed by synthesizing a nonlinear model-based minimum safety factor control algorithm that is designed to be integrated with the total-energy controller. The safety factor characterizes the pitch of the helical magnetic field and, hence, is a

function of the toroidal and poloidal components of the total field. During a plasma discharge, the toroidal field is approximately constant. Thus, the safety factor evolution primarily depends on the poloidal field. For an established plasma shape, which is regulated by the set of poloidal field coil currents, the toroidal current density predominantly governs the evolution of the equilibrium, hence the poloidal flux or, equivalently, the poloidal field. This implies that the control of the safety factor profile, and therefore its minimum q_{min}, is achieved by leveraging different noninductive current drive sources. One key contribution of this work is the development of a control-oriented model that accounts for the spatial evolution of the minimum safety factor. The 0D model is based on the magnetic diffusion equation [28] and predominantly characterizes q_{min} evolution. In this control-oriented model, the temperature and density profiles are modeled as constant profiles multiplied by time-varying scalars. Another significant contribution of this work is the synthesis of a nonlinear controller that treats not only the power but also the spatial aiming (or position) of each electron cyclotron current drive (ECCD) as controllable variables. An ECCD is a noninductive current drive that uses microwaves with frequencies equal to the electron cyclotron frequency, generated by a gyrotron, to drive current. In this work, the term "ECCD position" refers to the center of the region of plasma absorption of the microwaves. Tokamaks, like the DIII-D, are equipped with mirrors that can control the region of plasma absorption of the waves generated by the gyrotron. One can vary the mirror angles to vary the region of plasma absorption of these waves and, hence, the current deposition profile of the ECCD. Thus, the ECCD position can be used to adjust the current deposition in real time to improve the controllability of the minimum safety factor. The proposed nonlinear controller is based on optimized feedback linearization and is designed to incorporate the control objective of the plasma total energy controller that is running simultaneously. Computationally efficient algorithms of the proposed nonlinear controller are presented in this work to make real-time implementation feasible. The advantage of using moving ECCD is studied through nonlinear simulations that compare the proposed controller with a version of the fixed ECCD controller proposed in [20].

The following sections are organized as follows. Section 2 focuses on developing a nonlinear control-oriented model that governs the evolution of the minimum safety factor while accounting for its spatial movement. The proposed governing equation also models the effect of the ECCD position on the minimum safety factor dynamics. The nonlinear controller based on feedback linearization that treats ECCD position as one of the controllable variables is developed in Section 3. Nonlinear simulations that demonstrate the effectiveness of the proposed controller and highlight the advantages of moving ECCD are discussed in Section 4. Section 5 concludes the paper and lists potential future work. Finally, the theoretical and rigorous details involved in developing the model and the controller are given in Appendix.

2. Derivation of the control-oriented model

This section focuses on deriving the control-oriented model for the evolution of the minimum safety factor. The model is presented in terms of the poloidal flux gradient, a plasma parameter related to the safety factor. A partial differential equation (PDE) that governs the dynamics of the poloidal flux gradient is first derived. An interpolation-based model for the effect of ECCD position on the current deposition is then presented, and the spatially moving current deposition profile is incorporated into the PDE. The PDE is then simplified to a nonautonomous ordinary differential equation that governs the evolution of the minimum safety factor by tracking its location. The equation that governs the poloidal flux gradient error corresponding to a target minimum safety factor is finally derived. Since the dynamics of the minimum safety factor is affected by the plasma total energy, a model for the plasma total energy evolution is presented at the end of the section.
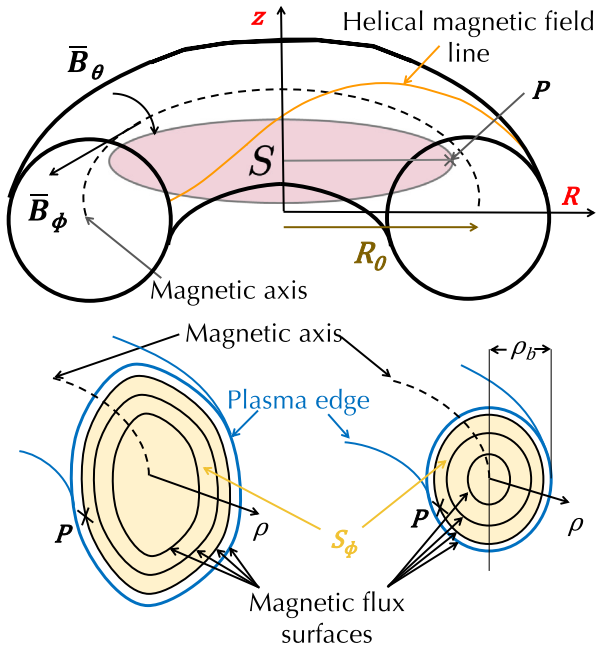
Fig. 1. Illustration of magnetic field lines and flux surfaces in a tokamak.
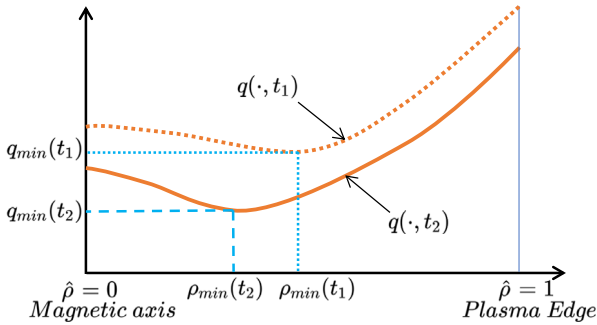
Fig. 2. Illustration of safety factor profile evolution during a typical tokamak discharge at times t_1 and t_2 with $t_1 < t_2$.

2.1. Normalized mean effective minor radius

The safety factor profile (and related parameters like the poloidal flux gradient) depends on a spatial variable and the time t. Any term that indexes the magnetic flux surfaces in the tokamak can be used as the spatial variable. The normalized mean effective minor radius, defined as $\hat{\rho} := \frac{\rho}{\rho_b}$, is used as the spatial variable in this work. In the definition, the term ρ is the mean effective minor radius that satisfies the equation $\Phi = B_{\phi,0}\pi\rho^2$, where Φ is the toroidal magnetic flux, and $B_{\phi,0}$ is the vacuum toroidal magnetic field at the major radius R_0 (refer to Fig. 1). The term ρ_b in the definition of $\hat{\rho}$ is the mean effective minor radius at the last closed magnetic flux surface.

2.2. Minimum safety factor

The safety factor characterizes the pitch of the helical magnetic field in the tokamak. It is defined as

$$q(\hat{\rho}, t) := -\frac{\partial \Phi/\partial \hat{\rho}}{\partial \Psi/\partial \hat{\rho}} = -\frac{\partial \Phi/\partial \hat{\rho}}{2\pi \partial \psi/\partial \hat{\rho}} = -\frac{B_{\phi,0}\rho_b^2\hat{\rho}}{\partial \psi/\partial \hat{\rho}}, \tag{1}$$

where Ψ is the poloidal magnetic flux and $\psi = \Psi/2\pi$ is the poloidal stream function. During a typical tokamak discharge, the safety factor profile q evolves with time. As a result, the minimum safety factor and

its location are continuously changing with time as illustrated in Fig. 2. In this work, the location of the minimum safety factor at any given time t is represented by $\hat{\rho}_{q_{min}}(t)$. Thus, the minimum safety factor $q_{min}(t)$ at a given time t satisfies the relation

$$q_{min}(t) := q(\hat{\rho}_{q_{min}}(t), t). \tag{2}$$

During a tokamak discharge, the safety factor profile can be obtained using real-time equilibrium reconstruction techniques [29]. As a result, one can determine q_{min} and $\hat{\rho}_{q_{min}}$ in real-time. In the following analysis, both values of $q_{min}(t)$ and $\hat{\rho}_{q_{min}}(t)$ at a given time t are assumed to be known.

2.3. Magnetic diffusion equation

The derivation of the control-oriented model starts with the consideration of the magnetic diffusion equation (MDE), which is a partial differential equation that governs the dynamics of the poloidal stream function [28]. It is given by

$$\frac{\partial \psi}{\partial t} = \frac{\eta}{\mu_0 \rho_b^2 \hat{F}^2} \frac{1}{\hat{\rho}} \frac{\partial}{\partial \hat{\rho}} \left(\hat{\rho} D_\psi \frac{\partial \psi}{\partial \hat{\rho}} \right) + R_0 \hat{H} \eta j_{ni} \tag{3}$$

subject to the Neumann boundary conditions

$$\frac{\partial \psi}{\partial \hat{\rho}}\bigg|_{\hat{\rho}=0} = 0, \qquad \frac{\partial \psi}{\partial \hat{\rho}}\bigg|_{\hat{\rho}=1} = -\underbrace{\frac{\mu_0}{2\pi} \frac{R_0}{\hat{G}_{\hat{\rho}=1}\hat{H}_{\hat{\rho}=1}}}_{k_{I_p}} I_p. \tag{4}$$

In the above equation, η is the plasma resistivity, μ_0 is the vacuum permeability, j_{ni} is the non-inductive current, R_0 is the tokamak major radius, and I_p is the plasma current. The functions $\hat{F} : \hat{\rho} \mapsto \hat{F}(\hat{\rho})$, $\hat{G} : \hat{\rho} \mapsto \hat{G}(\hat{\rho})$, $\hat{H} : \hat{\rho} \mapsto \hat{H}(\hat{\rho})$ are geometric factors pertaining to the magnetic configuration corresponding to a particular MHD equilibrium. The function D_ψ is defined as $D_\psi := \hat{F}\hat{G}\hat{H}$. The plasma resistivity η is modeled as a function of the electron temperature T_e of the form

$$\eta = \frac{Z_{eff}k_{sp}}{T_e^{3/2}}, \tag{5}$$

where Z_{eff} is the effective atomic number of the plasma ions, and k_{sp} is a constant spatial profile. The noninductive current j_{ni} is modeled as

$$j_{ni} = j_{aux} + j_{BS}, \tag{6}$$

$$j_{aux} = \sum_{i=1}^{N_{NBI}} j_{NBI,i}^{prof} \left(\frac{T_e^{\epsilon_{NBI}}}{n_e} \right) P_{NBI,i} + j_{EC}^{prof} \left(\frac{T_e^{\epsilon_{EC}}}{n_e} \right) P_{EC}, \tag{7}$$

$$j_{BS} = \frac{R_0}{\hat{F}} \left(\frac{\partial \psi}{\partial \hat{\rho}} \right)^{-1} \left(2\mathcal{L}_{31} T_e \frac{\partial n_e}{\partial \hat{\rho}} \right.$$
$$\left. + (2\mathcal{L}_{31} + \mathcal{L}_{32} + \alpha \mathcal{L}_{34}) n_e \frac{\partial T_e}{\partial \hat{\rho}} \right), \tag{8}$$

where j_{aux} and j_{BS} are the auxiliary drive and bootstrap current contributions to the total noninductive current, respectively. Note that the model for j_{aux} assumes N_{NBI} NBIs, and 1 ECCD. Even though the model assumes a single ECCD cluster in this work, the model and the controller can be extended to the case of multiple ECCD clusters with minimal changes. The terms $j_{NBI,i}^{prof}$ and j_{EC}^{prof} are the current depositions profiles of the ith NBI and ECCD, respectively, $P_{NBI,i}$ and P_{EC} are the ith NBI and ECCD powers, respectively, and n_e is the electron density. The constants ϵ_{NBI} and ϵ_{EC} characterize the efficiency of NBIs and ECCD, respectively. The functions α, $\mathcal{L}_{31}$, $\mathcal{L}_{32}$ and $\mathcal{L}_{34}$ are constant spatial profiles corresponding to a particular magnetic equilibrium.

Thus, the evolution of ψ depends on the evolution of T_e and n_e. To simplify the governing model of ψ, 0.5D control-oriented models for the electron density and electron temperature of the form

$$n_e(\hat{\rho}, t) = n_e^{prof}(\hat{\rho})\bar{n}_e(t), \tag{9}$$

$$T_e(\hat{\rho}, t) = T_e^{prof}(\hat{\rho})I_p(t)^\gamma P_{tot}(t)^\epsilon n_e(\hat{\rho}, t)^\zeta$$
$$= \hat{T}_e^{prof}(\hat{\rho})I_p(t)^\gamma P_{tot}(t)^\epsilon \bar{n}_e(t)^\zeta \tag{10}$$
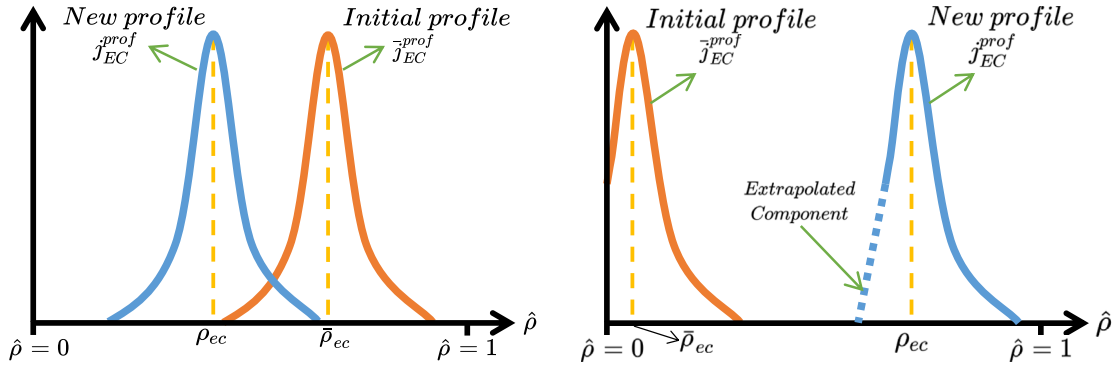
Fig. 3. The effect of EC position on the plasma dynamics is modeled by using a spatially translating current deposition profile.

are introduced. In the above models, γ, ϵ and ζ are constant scaling coefficients, T_e^{prof} and n_e^{prof} are fixed spatial profiles, $\hat{T}_e^{prof}(\hat{\rho}) = T_e^{prof}(\hat{\rho})(n_e^{prof}(\hat{\rho}))^\zeta$, P_{tot} is the total power, and $\bar{n}_e$ is the line-average electron density. The total power satisfies the relation

$$P_{tot} = \sum_{i=1}^{N_{NBI}} P_{NBI,i} + P_{EC}. \tag{11}$$

Note that the models for T_e and n_e presented above inherently assume that the temperature and the electron density profiles have fixed shapes, and their magnitudes scale with I_p, P_{tot} and $\bar{n}_e$ [30]. Thus, any changes in the temperature and electron-density profile shapes could increase the uncertainty in the control-oriented model. However, the new controller designed in the following section incorporates an integral action, which is effective in handling such model uncertainties as demonstrated to some extent in the numerical simulations.

In this work, the minimum safety factor regulation is achieved by actively modulating the values of auxiliary powers $P_{NBI,i}$, P_{EC} and ECCD position ρ_{ec}. In contrast, the minimum safety factor controller considers the terms $\bar{n}_e$, I_p, and P_{tot} as prescribed inputs. The assumption is that parallel controllers (designed to control other plasma properties) prescribe these values simultaneously at each time t. For instance, the total energy controller, discussed in Section 3.2, prescribes the value of P_{tot}. The minimum safety factor controller then chooses its corresponding inputs such that the sum of all auxiliary powers is equal to the prescribed value of P_{tot}.

From (1), it is clear that the safety factor depends on the gradient of the poloidal stream function. Thus, using a control-oriented model that governs the evolution of the poloidal flux gradient $\theta := \frac{\partial \psi}{\partial \hat{\rho}}$ makes the control synthesis simpler. Hence, after incorporating (5), (6), (7), (8), (10) and (9) into (3), the spatial derivative of the resulting equation is taken on both sides. This results in a partial differential equation (that is defined in terms of θ) of the form

$$\dot{\theta} = \left(h_{\eta,1}\theta'' + h_{\eta,2}\theta' + h_{\eta,3}\theta\right)u_\eta + \sum_{i=1}^{N_{NBI}} h_{NBI,i}u_{NBI,i}$$
$$+ h_{EC}u_{EC} + \left(h_{BS,1}\frac{1}{\theta} - h_{BS,2}\frac{\theta'}{\theta^2}\right)u_{BS}, \tag{12}$$

subject to $\theta(0,t) = 0, \theta(1,t) = -k_{I_p}I_p$. In the above equation, the notations $(\dot{\cdot})$ and $(\cdot)'$ represent the derivative with respect to time t and spatial variable $\hat{\rho}$, respectively. The steps involved in deriving the above equation and the explicit definitions of the spatial functions $h_{(\cdot)}$ and virtual inputs $u_{(\cdot)}$ are given in Appendix A.

2.4. Modeling the effect of ECCD position on the polidal flux gradient dynamics

The infinite-dimensional PDE derived in the previous subsection does not consider the explicit effect of the ECCD position on the plasma dynamics. The focus of this subsection to eliminate the assumption that

the ECCD position is static and to incorporate its effect into the model. As mentioned earlier, the term j_{EC}^{prof} accounts for the current deposition profile of the ECCD. Varying the ECCD position changes j_{EC}^{prof}, which in turn varies h_{EC} in (12). Suppose that the ECCD is placed at $\bar{\rho}_{ec}$ initially and j_{EC}^{prof} is the current deposition profile corresponding to this initial position. Now, assume that the ECCD is shifted to a new position ρ_{ec}. Then, the current deposition profile $\bar{j}_{EC}$ of the ECCD corresponding to the new position is obtained by shifting the center of the original profile. Mathematically, this is given by

$$\bar{j}_{EC}^{prof}(\rho_{ec}, \hat{\rho}) := j_{EC}^{prof}(\hat{\rho} + \bar{\rho}_{ec} - \rho_{ec}). \tag{13}$$

Fig. 3 (left subfigure) gives an intuitive illustration of how the new current deposition profile is created from the initial profile. In certain cases, the initial ECCD position $\bar{\rho}_{ec}$ can be such that the value of current deposition profile j_{EC}^{prof} at spatial boundaries ($\hat{\rho} = 0$ and $\hat{\rho} = 1$) is not equal to zero. In such cases, extrapolation is used. The need for extrapolation in such cases is illustrated in Fig. 3 (right subfigure). From (13), note that the new current deposition profile $\bar{j}_{EC}^{prof}$ depends on the spatial variable $\hat{\rho}$ and the ECCD position ρ_{ec}.

The effect of the ECCD position on the plasma dynamics is modeled in this work by replacing h_{EC} (defined in Appendix A) in the control model (12) with

$$\bar{h}_{EC}(\rho_{ec}, \hat{\rho}) := (\bar{g}_{EC}(\rho_{ec}, \hat{\rho}))', \tag{14}$$

where

$$\bar{g}_{EC}(\rho_{ec}, \hat{\rho}) := \hat{g}_\eta(\hat{\rho})R_0\hat{H}(\hat{\rho})\hat{\bar{g}}_{EC}(\rho_{ec}, \hat{\rho}),$$
$$\hat{\bar{g}}_{EC}(\rho_{ec}, \hat{\rho}) := \bar{j}_{EC}^{prof}(\rho_{ec}, \hat{\rho})\left(T_e^{prof}(\hat{\rho})\right)^{\epsilon_{EC}}\left(n_e^{prof}(\hat{\rho})\right)^{(\zeta\epsilon_{EC}-1)}.$$

Thus, the new partial differential equation that governs the evolution of the poloidal flux gradient and incorporates the effect of the ECCD position is given by

$$\dot{\theta} = \left(h_{\eta,1}\theta'' + h_{\eta,2}\theta' + h_{\eta,3}\theta\right)u_\eta + \sum_{i=1}^{N_{NBI}} h_{NBI,i}u_{NBI,i}$$
$$+ \bar{h}_{EC}(\rho_{ec}, \hat{\rho})u_{EC} + \left(h_{BS,1}\frac{1}{\theta} - h_{BS,2}\frac{\theta'}{\theta^2}\right)u_{BS} \tag{15}$$

subject to $\theta(0,t) = 0, \theta(1,t) = -k_{I_p}I_p$.

2.5. Model simplification to track the minimum safety factor

The model developed in the previous subsection considers the whole poloidal flux gradient profile. In other words, it does not track the dynamics of minimum safety factor (a spatially varying term). Such a model is too complicated for the minimum safety factor control problem, which is the primary emphasis of this work. To simplify the model, the spatial component of the PDE in (15) is evaluated at q_{min} location $\hat{\rho}_{q_{min}}$. This results in a non-autonomous ordinary differential equation of the form

$$\dot\theta_{q_{min}}(t) =$$

$$\underbrace{\left(h_{\eta,1}^{min}(t)\theta_{q_{min}}''(t) + h_{\eta,2}^{min}(t)\theta_{q_{min}}'(t) + h_{\eta,3}^{min}(t)\theta_{q_{min}}(t)\right)u_\eta(t)}_{c_1}$$

$$+ \sum_{i=1}^{N_{NBI}} h_{NBI,i}^{min}(t)u_{NBI,i}(t) + \bar h_{EC}^{min}(\rho_{ec},t)u_{EC}(t)$$

$$+ \underbrace{\left(h_{BS,1}^{min}(t)\frac{1}{\theta_{q_{min}}(t)} - h_{BS,2}^{min}(t)\frac{\theta_{q_{min}}'(t)}{\left(\theta_{q_{min}}(t)\right)^2}\right)u_{BS}(t)}_{c_2}, \tag{16}$$

where

$$\theta_{q_{min}}(t) := \theta(\hat\rho_{q_{min}}(t),t), \tag{17}$$

$$\theta_{q_{min}}'(t) := \theta'(\hat\rho_{q_{min}}(t),t), \tag{18}$$

$$\theta_{q_{min}}''(t) := \theta''(\hat\rho_{q_{min}}(t),t), \tag{19}$$

$$h_{(\cdot)}^{min}(t) := h_{(\cdot)} \circ \hat\rho_{q_{min}}(t), \tag{20}$$

$$\bar h_{EC}^{min}(\rho_{ec},t) := \bar h_{EC}(\rho_{ec},\hat\rho_{q_{min}}(t)). \tag{21}$$

2.6. Poloidal flux gradient error equation

Suppose a target minimum safety factor $\bar q_{min}$ is given. The corresponding target poloidal flux gradient is obtained using the equation

$$\bar\theta_{q_{min}}(t) = -\frac{B_{\phi,0}\rho_b^2 \hat\rho_{q_{min}}(t)}{\bar q_{min}(t)}. \tag{22}$$

Thus, the objective of the controller is to choose (feedback components of) $P_{NBI,i}$, P_{EC} and ρ_{ec} to drive the error $\tilde\theta_{q_{min}} = \theta_{q_{min}} - \bar\theta_{q_{min}}$ to 0. Thus, from the perspective of control design, it is more convenient to use a model based on $\tilde\theta_{q_{min}}$, feedback components of actual inputs $P_{NBI,i}$, P_{EC} instead of a model based on $\theta_{q_{min}}$ and virtual inputs $u_{NBI,i}$, u_{EC}. To enable this redefinition of the control-oriented model, two new time-dependent functions $h_{NBI,i}^{*,min}$ and $\bar h_{EC}^{*,min}$ are defined as

$$h_{NBI,i}^{*,min} := h_{NBI,i}^{min}(I_p^\gamma P_{tot}^\epsilon \bar n_e^\zeta)^{(-3/2+\zeta_{NBI})}\bar n_e^{-1}, \tag{23}$$

$$\bar h_{EC}^{*,min} := \bar h_{EC}^{min}(I_p^\gamma P_{tot}^\epsilon \bar n_e^\zeta)^{(-3/2+\zeta_{EC})}\bar n_e^{-1}, \tag{24}$$

where the functions $h_{NBI,i}^{min} : t \mapsto h_{NBI,i}^{min}(t)$ and $\bar h_{EC}^{min} : (\rho_{ec},t) \mapsto \bar h_{EC}^{min}(\rho_{ec},t)$ are defined above. Thus, one can replace virtual inputs in (16) with the actual inputs using these equations. Now suppose that the actual inputs $P_{NBI,i}$ and P_{EC} have feedforward and feedback terms such that $P_{NBI,i} = P_{NBI,ff,i} + P_{NBI,fb,i}$ and $P_{EC} = P_{EC,ff} + P_{EC,fb}$, where the subscripts ff and fb correspond to the feedforward and feedback components, respectively. With these considerations, one can write the error equations as

$$\dot{\tilde\theta}_{q_{min}}(t) = c_1(t) + c_2(t) + h(\rho_{ec},t)^T u_{ff}(t)$$
$$+ h(\rho_{ec},t)^T u_{fb}(t) - \dot{\bar\theta}_{q_{min}}(t), \tag{25}$$

where

$$h(\rho_{ec},\cdot) = \begin{bmatrix} h_{NBI,1}^{*,min}, & \cdots, & h_{NBI,N_{NBI}}^{*,min}, & \bar h_{EC}^{*,min}(\rho_{ec},\cdot) \end{bmatrix}^T,$$

$$u_{ff} = \begin{bmatrix} P_{NBI,ff,1}, & \cdots, & P_{NBI,ff,N_{NBI}}, & P_{EC,ff} \end{bmatrix}^T,$$

$$u_{fb} = \begin{bmatrix} P_{NBI,fb,1}, & \cdots, & P_{NBI,fb,N_{NBI}}, & P_{EC,fb} \end{bmatrix}^T,$$

and the functions c_1, c_2 are defined in (16).

2.7. Plasma total energy evolution model

As discussed above, the plasma total energy is prescribed by a controller running simultaneously to the minimum safety factor controller. This section aims to present the control-oriented model for the evolution of the plasma total energy W. It is modeled by the one-dimensional ordinary differential equation of the form

$$\dot W(t) = -\frac{W(t)}{\tau_E(t)} + P_{tot}(t). \tag{26}$$

In the above equation, the term τ_E is the energy confinement time and is calculated using the $IPB98(y,2)$ scaling law [31]. Suppose a target plasma total energy $\bar W$ is given. Then the evolution of the error $\tilde W = W - \bar W$ is governed by

$$\dot{\tilde W} = -\frac{W}{\tau_E} + P_{tot} - \dot{\bar W}. \tag{27}$$

3. Minimum safety factor control synthesis

This section aims to develop nonlinear plasma total energy W and minimum safety factor q_{min} controllers. The plasma total energy controller prescribes the total power P_{tot} to drive the error $\tilde W$ to 0. According to (11), the prescribed total power imposes an algebraic constraint on the minimum safety factor controller, which prescribes the auxiliary powers and the ECCD position to drive the error $\tilde\theta_{q_{min}}$ to 0. This work uses an algorithm based on feedback linearization to achieve the control objectives. The W controller first determines the value of P_{tot} to cancel the nonlinearities in (27) and track the target $\bar W$. The q_{min} controller then chooses the value of auxiliary inputs and ECCD position while accounting for the algebraic constraint imposed by the W controller and (11). The robust version of q_{min} controller, introduced in [20], is presented in Appendix C.

3.1. Feedback linearization

Feedback linearization is a nonlinear control algorithm that works on the principle of canceling the nonlinearities in the model. The resulting model is linear, which can be controlled using a linear control algorithm. Fig. 4 shows a block diagram of the closed-loop system. Note that both the linear controller and the nonlinearity cancellation blocks in the block diagram form the feedback linearization controller. The linear controller prescribes a virtual input v to the linearized model based on the state error $\tilde x$. The nonlinearity cancellation block prescribes the actual power v_{act} to cancel the nonlinearities in (25). The following subsections discuss how feedback linearization is used in this work to drive the plasma total energy and the minimum safety factor to the desired targets.

3.2. Plasma total energy controller

The objective of the W controller is to choose the actual input $v_{act} = P_{tot}$ to drive the state error $\tilde x = \tilde W$ to 0. The state error $\tilde W$ determines the virtual input v by the relation

$$v = -K_{W,p}\tilde W - K_{W,I}\int_{t_0}^t \tilde W dt, \tag{28}$$

where $K_{W,p}$ and $K_{W,I}$ are predefined control parameters and t_0 is the initial time. The actual input P_{tot} is related to the virtual input v by the equation

$$v = -\frac{W}{\tau_E} + P_{tot} - \dot{\bar W}. \tag{29}$$

Substituting (28) and (29) into (27) gives the linear equation

$$\dot{\tilde W} = -K_{W,p}\tilde W - K_{W,I}\int_{t_0}^t \tilde W dt. \tag{30}$$

Using Lyapunov analysis (similar to the one shown in Appendix B), it can be shown that the above system is asymptotically stable, i.e., the error $\tilde W$ converges to 0 as $t \to \infty$. Thus, the control objective is achieved by choosing the feedback component of the actual input $P_{tot,fb}$ as

$$P_{tot,fb} = -K_{W,p}\tilde W - K_{W,I}\int_{t_0}^t \tilde W dt + \frac{W}{\tau_E} - P_{tot,ff} + \dot{\bar W}. \tag{31}$$

In the above equation, the term $P_{tot,ff}$ represents the feedforward component of the total power.
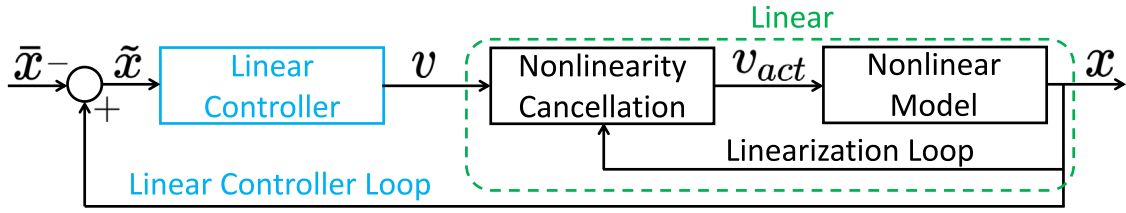
Fig. 4. Feedback linearization controller block diagram.
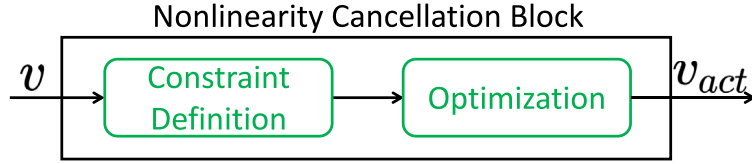
Fig. 5. Components of a feedback linearization block.

3.3. Minimum safety factor controller synthesis

For the minimum safety factor controller, the state error is $\tilde{x} = \tilde{\theta}_{q_{min}}$. The actual inputs v_{act} for this controller are the auxiliary powers u_{fb} and the ECCD position ρ_{ec}. The nonlinearity cancellation in the $\tilde{\theta}_{q_{min}}$ model (25) is achieved by ensuring that the virtual input v satisfies the constraint

$$v = c_1(t) + c_2(t) + h(\rho_{ec}(t), t)^T u_{ff}(t)$$
$$+ h(\rho_{ec}(t), t)^T u_{fb}(t) - \dot{\tilde{\theta}}_{q_{min}}(t). \tag{32}$$

The linear controller (refer to Fig. 4) prescribes a value for the virtual input v based on the error $\tilde{\theta}_{q_{min}}$. The linear control law used in this work is given by

$$v = -K_p \tilde{\theta}_{q_{min}} - K_I \int_{t_0}^{t} \tilde{\theta}_{q_{min}} dt \tag{33}$$

with controller gains $K_p > 0$, $K_I > 0$. Combining (25), (32) and (33) results in the closed-loop linear system

$$\dot{\tilde{\theta}}_{q_{min}} = -K_p \tilde{\theta}_{q_{min}} - K_I \int_{t_0}^{t} \tilde{\theta}_{q_{min}} dt. \tag{34}$$

Stability analysis, discussed in Appendix B, shows that the above controller can drive the error to 0 asymptotically under certain hypotheses. Thus, by choosing auxiliary powers u_{fb} and ECCD position ρ_{ec} such that (32) and (33) are simultaneously satisfied achieves the desired control objective. Such a selection of controllable variables is achieved through optimization, which is discussed below.

3.4. Optimal allocation of physical actuators

As discussed in the previous sections, the critical step in feedback linearization is nonlinearity cancellation. Fig. 5 shows the steps involved in the nonlinearity cancellation block of the controller. The constraint definition block defines the relation (given in (32)) between the virtual input u and actual inputs u_{fb}. Since there is only one virtual input (defined by the linear control law (33)), and $N_{NBI} + 1$ auxiliary drives, there is no unique way to select the actual inputs u_{fb} to satisfy the constraint given in (32). Furthermore, the total power, defined by (11), introduces an additional constraint on the auxiliary powers. This work uses optimization to select a unique set of actual feedback inputs that satisfy all the above-mentioned constraints. The optimization problem is formulated as follows: for each time t,

$$\underset{u(t),\rho_{ec}(t)}{\mathrm{argmin}} f(u(t)) = \underset{u(t),\rho_{ec}(t)}{\mathrm{argmin}} u^T(t) Q u(t) \tag{35}$$

subject to the constraints

$$g_1(\rho_{ec}(t), u(t), t) := \hat{h}^T(\rho_{ec}(t), t) u(t) + b_1(\rho_{ec}(t), t) = 0, \tag{36}$$

$$g_2(u(t), t) := \hat{\mathbb{1}}^T u(t) + b_2(t) = 0, \tag{37}$$

$$u(t) \in \Gamma \times (-\infty, \infty) \times (-\infty, \infty), \text{ and} \tag{38}$$

$$\rho_{ec} \in [0, 1]. \tag{39}$$

In the above formulation, "argmin" refers to the values of $u(t)$ and $\rho_{ec}(t)$ that minimize the cost function f,

$$u = \begin{bmatrix} u_{fb}^T & s_1 & s_2 \end{bmatrix}^T, \tag{40}$$

$$\hat{h}(\rho_{ec}, t) = \begin{bmatrix} h^T(\rho_{ec}, t) & 1 & 0 \end{bmatrix}^T, \tag{41}$$

$$\hat{\mathbb{1}} = \begin{bmatrix} \mathbb{1}^T & 0 & 1 \end{bmatrix}^T, \tag{42}$$

$$\mathbb{1} = \begin{bmatrix} 1 & \cdots & 1 \end{bmatrix}^T, \tag{43}$$

$$b_1(\rho_{ec}, \cdot) = K_p \tilde{\theta}_{q_{min}} + K_I \int_{t_0}^{t} \tilde{\theta}_{q_{min}} dt - \dot{\tilde{\theta}}_{q_{min}}$$
$$+ c_1 + c_2 + h^T(\rho_{ec}, \cdot) u_{ff}, \tag{44}$$

$$b_2 = -P_{tot} + \mathbb{1}^T u_{ff}. \tag{45}$$

Note that the auxiliary powers appear in the cost function and the constraints. However, the ECCD position appears explicitly only in the constraints. The set $\Gamma \subset \mathbb{R}^{N_{NBI}+1}$ is defined as

$$\Gamma = [\underline{\gamma}_1, \bar{\gamma}_1] \times \cdots \times [\underline{\gamma}_{N_{NBI}+1}, \bar{\gamma}_{N_{NBI}+1}] \subset \mathbb{R}^{N_{NBI}+1}, \tag{46}$$

where $\underline{\gamma}_i$, $\bar{\gamma}_i$ represent the lower and upper saturation limits of ith auxiliary drive. The optimization problem may not have an exact solution within the input bounds (38) and (39) such that the constraints (36) and (37) are satisfied. One way to ensure the existence of a solution is the inclusion of "slack" variables (s_1 and s_2 in the above equations) that are allowed to take values in an unbounded set $(-\infty, \infty) \times (-\infty, \infty)$. Consequently, the slack variables s_1 and s_2 give a measure of constraints violation ((36) and (37), respectively) to ensure the existence of solution such that $u_{fb} \in \Gamma$ and $\rho_{ec} \in [0, 1]$. It is important to ensure that the solution to the optimization problem is such that the constraint violation is minimal. This is achieved by choosing the matrix Q in the cost function as a diagonal matrix of the form $Q = diag(q_1, \ldots, q_{N_{NBI}+1}, q_{s_1}, q_{s_2})$, $q_{s_1}, q_{s_2} \gg q_i > 0$ for $i = 1, \ldots, N_{NBI} + 1$. Such a selection of Q matrix ensures that the cost of violating the constraint is significant.

Real-time (nonlinear) optimization can be computationally expensive. Furthermore, incorporating auxiliary drive saturation limits into optimization increases the complexity. To make practical implementation feasible, optimization is carried out in three steps. First, the optimization problem for a fixed ECCD position is solved. Next, actuator saturation limits and the moving ECCD are incorporated into the optimization process in Section 3.4.2.

3.4.1. Optimization for fixed ECCD case without saturation limits

Suppose the actuator saturation limits ((38) and (39)) are ignored and the ECCD is fixed at $\hat{\rho} = \hat{\rho}_{ec}$. Define $\hat{h}^*$ as $\hat{h}^*(t) := \hat{h}(\hat{\rho}_{ec}, t)$. The optimization formulated above simplifies to minimizing a quadratic cost function subject to two linear constraints. Using Lagrange multiplier theorem, it can be shown that the solution u^* of the simplified optimization problem is given by the formula

$$u^* = \frac{1}{2}Q^{-1}\begin{bmatrix}\hat{h}^* & \hat{\mathbb{1}}\end{bmatrix}\Lambda, \tag{47}$$

where Λ satisfies the linear equation

$$\underbrace{\begin{bmatrix}\hat{h}^{*T}Q^{-1}\hat{h}^* & \hat{h}^{*T}Q^{-1}\hat{\mathbb{1}} \\ \hat{\mathbb{1}}^{T}Q^{-1}\hat{h}^* & \hat{\mathbb{1}}Q^{-1}\hat{\mathbb{1}}\end{bmatrix}}_{\mathbb{A}}\underbrace{\begin{Bmatrix}\lambda_1^* \\ \lambda_2^*\end{Bmatrix}}_{\Lambda} = \underbrace{\begin{bmatrix}-2b_1 \\ -2b_2\end{bmatrix}}_{b}. \tag{48}$$

All detailed steps involved in deriving the above equation is given in Appendix D. Since there are two constraints that are linear in inputs u, at least two auxiliary drives are required to ensure the existence of solution to the simplified optimization problem. This in turn implies $N_{NBI} \geq 1$.

3.4.2. Incorporation of saturation limits and moving ECCD into control algorithm

To include the actuator saturation limits, one can add inequality constraints explicitly. However, this makes the optimization algorithm convoluted. If (47) returns a feedback input value that is outside the set Γ, then the solution of the optimization problem with saturation constraints is achieved at the boundary of the set Γ. For this problem, the boundary is nothing but the saturated values of the inputs. Algorithm 1, given in Appendix E, uses this fact to iteratively arrive at the solution of the optimization problem with actuator saturation limits.

The following example gives an intuitive illustration of the algorithm. Suppose 2 NBIs and 1 ECCD are allocated for safety factor minimum control. Also suppose that the lower and upper saturation limits of all three actuators are 0 MW and 5 MW, respectively. At any given time t, if u^* calculated by (47) satisfies the saturation limits, then the algorithm returns u^*. On the other hand, if u^* is such that both NBIs satisfy the saturation limits but the ECCD power is 6 MW, then the algorithm sets the value of ECCD power as 5 MW and reformulates the optimization problem in terms of the NBI actuator powers. This process is repeated until all the inputs satisfy the actuator saturation limits.

The next step is to include the ECCD position as one of the variables in the optimization problem. Algorithm 2, presented in Appendix F, gives a computationally efficient algorithm to determine the optimal ECCD position. In Algorithm 2, the ECCD position ρ_{ec} is assumed to be fixed at $\hat{\rho}_{ec}$. Suppose δ is the maximum possible distance the ECCD can move from its position ρ_{ec} at a given time step t_k. Define Ω^k as the finite set of possible positions the ECCD can take at the next time step. Algorithm 2 solves the optimization problem corresponding to each ECCD position in the set Ω_k (by implementing Algorithm 1) and computes the cost function corresponding to each ECCD position. The optimal ECCD position $\rho_{ec}^{*,k}$ is the ECCD position $\rho_{ec} \in \Omega_k$ corresponding to the least cost function value.

4. Control testing via numerical simulations

The control algorithm developed in Section 3 is tested for a DIII-D tokamak scenario using numerical simulations in the Control Oriented Transport SIMulator (COTSIM). In COTSIM, the 1D magnetic diffusion equation, the electron-heat-transport equation, and the semi-empirical Bohm/Gyro-Bohm model are used for simulating the plasma dynamics [32]. Furthermore, the evolution models used in COTSIM are more complicated than those used in the control design. As a result, testing the algorithms developed in this work in COTSIM serves as a good step before proceeding to actual experiments. In the simulations, two NBIs and one ECCD are considered for minimum safety factor control. The simulations use data from DIII-D shot 147 634 [33]. In particular, the targets are generated using the inputs data from shot 147 634. In the simulations, the values of $P_{NBI,1}$ (on-axis NBI cluster), $P_{NBI,2}$ (off-axis NBI cluster) and P_{EC} are allowed to vary in the closed intervals [0 MW, 12 MW], [0 MW, 6 MW] and [0 MW, 4.5 MW], respectively. Fig. 6 shows the current depositions profiles of these actuators. The effectiveness of the controller was tested for multiple cases. The simulation results of two different cases, with two different feedforward input combinations and initial ECCD positions, are presented below. The results for fixed and moving ECCD studies are presented in each of the two cases. A non-robust version of the controller proposed in [20] was used for the fixed ECCD case. The controller algorithm for this case is similar to Algorithm 2, with the only difference being that the set Ω_k is chosen as a singleton set of the fixed ECCD position at every time step t_k.

4.1. Case 1

Since the ECCD position is determined only by the feedback controller, $P_{EC,ff}$ cannot be determined a priori. In the first case, the feedforward EC power $P_{EC,ff}$ is selected as $P_{EC,ff} = 0$. This difference in the EC power in the feedforward and target shots results in the deviation of the plasma total energy and the minimum safety factor from the targets. The results of the W controller when the ECCD is fixed are given in Fig. 7. Activating the controller makes the system track the target $\overline{W}$. As mentioned previously, the total power P_{tot} power of the feedforward+feedback case (refer to right subfigure of Fig. 7) determined by the W controller imposes a constraint on the minimum safety factor controller. Figs. 8, 9 show the simulations results of the fixed ECCD case. As evident from the figures, the controller is able to track the target even when the ECCD is fixed. Fig. 8 also shows the ECCD position, which is fixed in this case, and the minimum safety factor location $\hat{\rho}_{q_{min}}$. Fig. 11 shows the feedforward-only and feedforward+feedback inputs corresponding to the minimum safety factor trajectories shown in Fig. 8. The figure illustrates that $P_{NBI,2}$ saturates when the controller is activated. Thus, when the control algorithm is implemented, the original solution of the optimization problem without saturation limits, discussed in Section 3.4.1, is such that $P_{NBI,1} \in [0\text{ MW}, 12\text{ MW}]$, $P_{EC} \in [0\text{ MW}, 4.5\text{ MW}]$, but $P_{NBI,2} > 6$ MW. Thus, Algorithms 1 and 2 set the value of $P_{NBI,2}$ at 6 MW and solved the optimization problem with only $P_{NBI,1}$ and P_{EC}. As shown in Fig. 11, the new solution of the reformulated optimization problem results in a spike in the ECCD power P_{EC}. Due to the inherent coupling of the plasma total power evolution and minimum safety factor evolution, the spike in ECCD power results in the deviation of W from its target (refer to the central subfigure of Fig. 7).

The evolution of W and the corresponding total power for the feedforward only and feedforward+feedback cases when ρ_{ec} is allowed to vary is shown in Fig. 12. As evident from the figure, the controller tracks the given target. Figs. 13, 14 present the q_{min}, ρ_{ec}, $\hat{\rho}_{q_{min}}$ and q profile values for the moving ECCD case, i.e., for the case when Algorithm 1 is implemented without any modifications. Figs. 13 and 14 show that the controller makes the system track the target. Furthermore, it can be seen that the optimal ECCD position is roughly located at $\hat{\rho}_{q_{min}} + 0.115$. Since the ECCD position is moved towards $\hat{\rho}_{q_{min}}$ in real-time, the controller does not need to rely heavily on the NBIs to drive current at around $\hat{\rho}_{q_{min}}$, which prevents $P_{NBI,2}$ from entering saturation and P_{EC} from spiking at the same time, as shown in Fig. 16. As a result, unlike the fixed ECCD case, there are no spikes in δW evolution (as shown in the central subfigure of Fig. 12).

Figs. 10 and 15 show the temperature profiles predicted by the simulator and controller-synthesis models. As mentioned earlier, the simulators use a 1D electron-heat-transport equation. On the other hand, the controller synthesis relied on a 0.5D temperature model with fixed shapes (refer to (10)). Thus, the 1D and 0.5D temperature
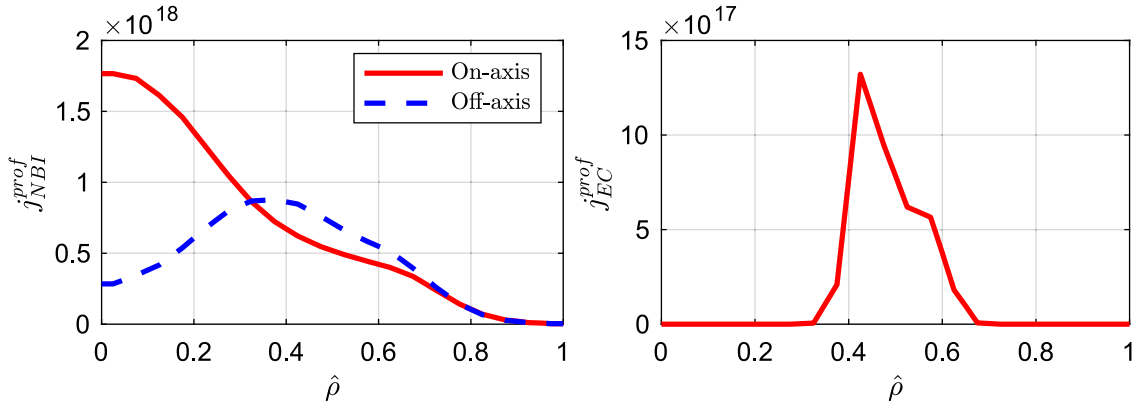
Fig. 6. Auxiliary drive current deposition profiles: NBIs (left), ECCD (right).
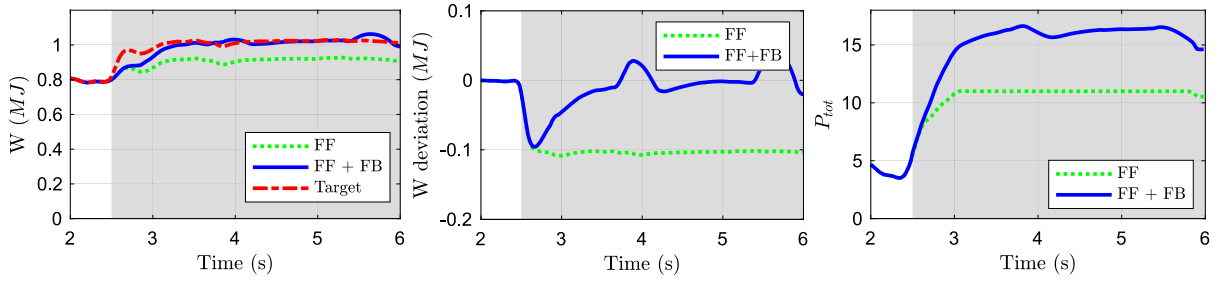
Fig. 7. Case 1 - fixed ECCD: W (left), $\tilde{W}$ (center), P_{tot} (right).
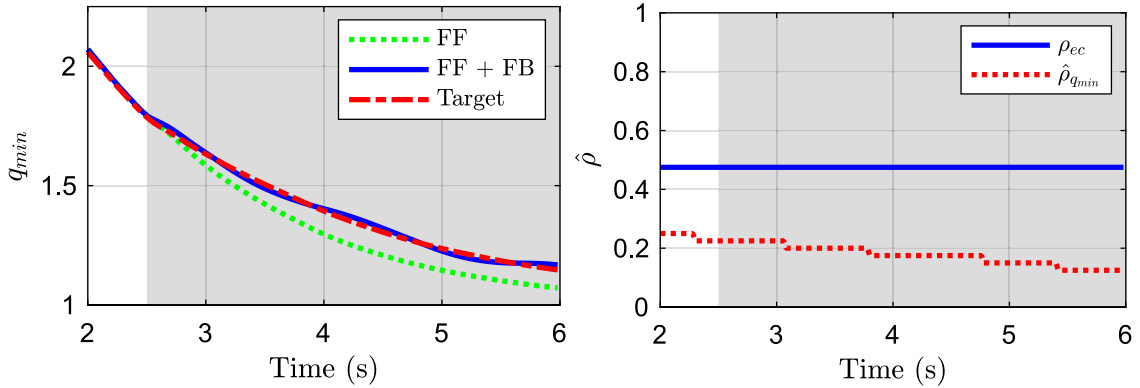
Fig. 8. Case 1 - fixed ECCD: q_{min} evolution (left), ECCD position (right).
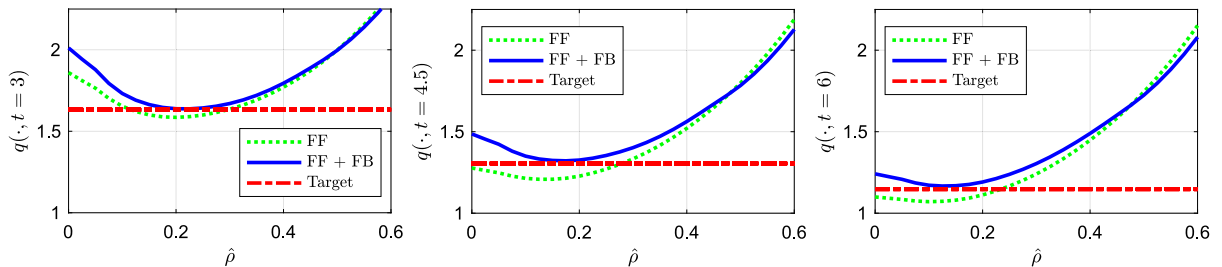
Fig. 9. Case 1 - fixed ECCD: safety factor profile - $t = 3$ s (left), $t = 4.5$ s (center), $t = 6$ s (right).

profile discrepancy translates to uncertainty in the control-oriented q_{min} model. However, the closed-loop plots show that the controller is able to eliminate the effect of model uncertainty and track the given target in both fixed and moving ECCD cases.

The cost value at each time instant t is shown in Fig. 17. The sudden increase in the P_{EC} value for the fixed ECCD case is evident from the

figure. Since the optimization problem is solved at each time instant independently, inputs that are optimal at one instant can result in a suboptimal performance at the latter instants. This is evident from the fact that the cost value for the moving ECCD case is greater than that of the fixed ECCD case at certain time instants. Hence, to compare overall performance of both cases, a cumulative cost $\hat{J}(t) := \int_0^t J(u(\tau))d\tau$ is
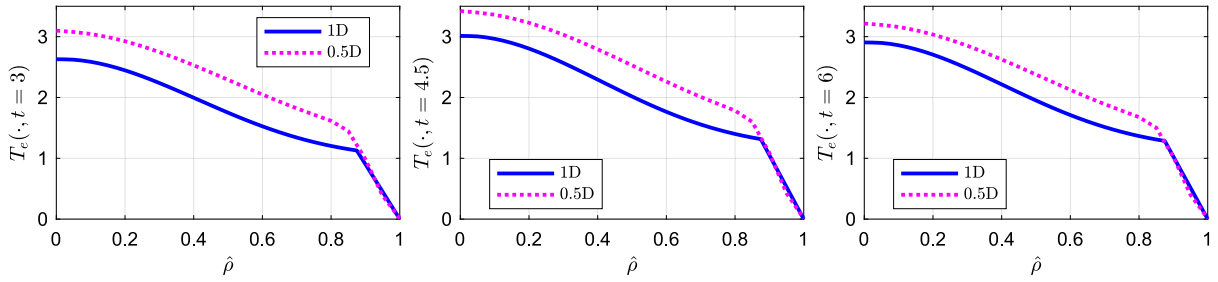
Fig. 10. Case 1 - fixed ECCD: electron temperature profile as predicted by the simulator (1D) and synthesis (0.5D) models - $t = 3$ s (left), $t = 4.5$ s (center), $t = 6$ s (right).
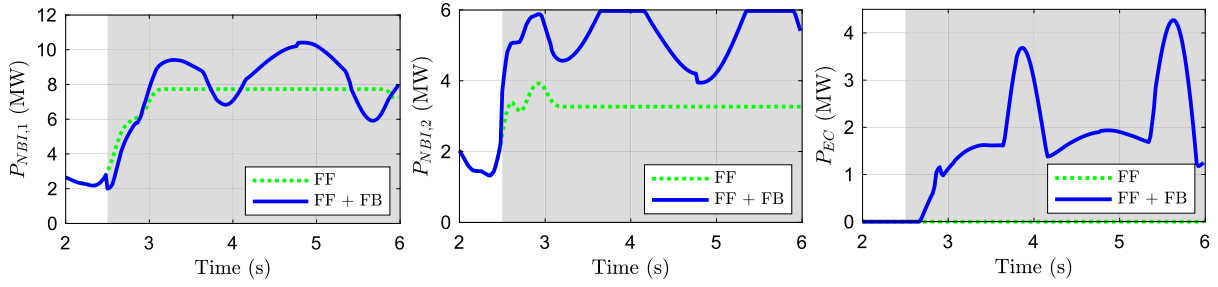
Fig. 11. Case 1 - fixed ECCD: Auxiliary powers - $P_{NBI,1}$ (left), $P_{NBI,2}$ (center), P_{EC} (right).
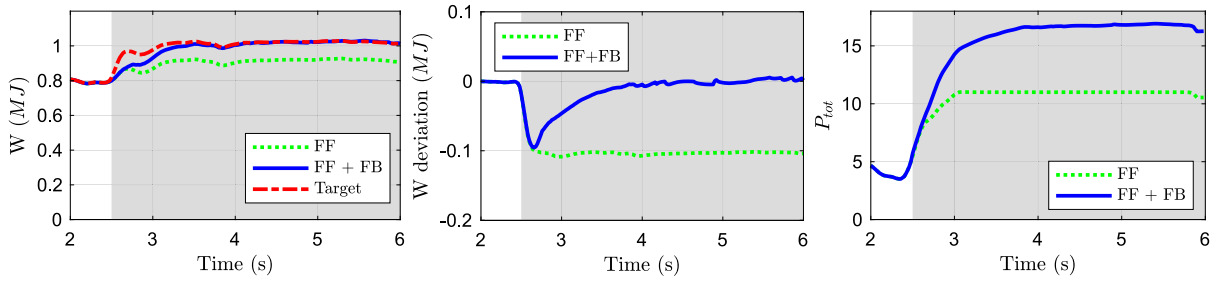
Fig. 12. Case 1 - moving ECCD: W (left), $\tilde{W}$ (center), P_{tot} (right).
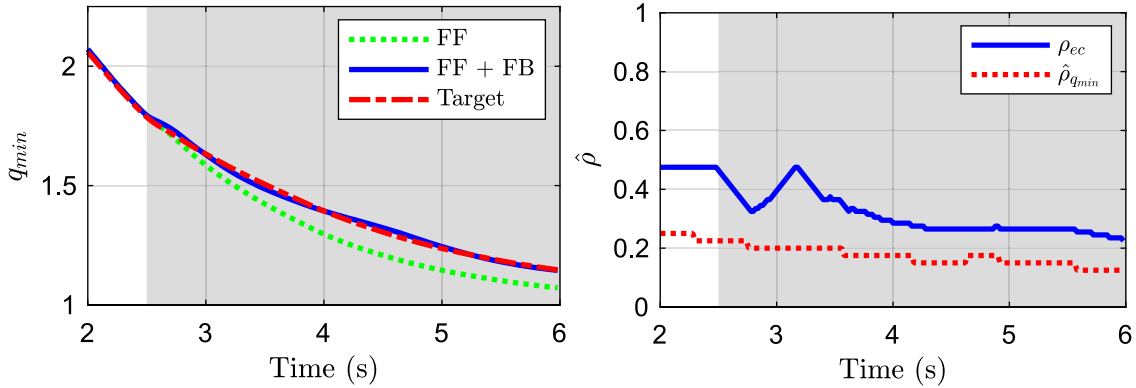
Fig. 13. Case 1 - moving ECCD: q_{min} evolution (left), ECCD position (right).

used. Fig. 17 also shows the cumulative costs of the fixed and moving ECCD cases. The cumulative costs $\hat{J}(t_{end})$ at the simulation end time t_{end} for the fixed and moving ECCD cases are 1.9720×10^3 and 1.6069×10^3, respectively. Thus, controlling the ECCD position results in a lower cumulative cost for the given set of simulation parameters.

4.2. Case 2

In the second case, the feedforward inputs are selected as $P_{NBI,1,ff} = 0.75 P_{NBI,1,tar}$, $P_{NBI,2,ff} = 0.5 P_{NBI,2,tar}$, $P_{EC,ff} = 0$, where $P_{NBI,1,tar}$

and $P_{NBI,2,tar}$ are the auxiliary powers corresponding to the target profile. The results corresponding to the fixed ECCD case are given in Figs. 18, 19, 20, 21 and 22. Fig. 18 shows that the W controller tracks the target $\overline{W}$. The initial discrepancy between the system's state W and the target $\overline{W}$ when the controller is activated causes a spike in the feedforward+feedback input P_{tot}. However, after this initial overshoot, the error slowly converges to 0 (refer to the central subfigure in Fig. 18). Figs. 19 and 20 show that the minimum safety factor controller tracks the given target. The evolution of the electron temperature profile with and without the feedback controller is shown
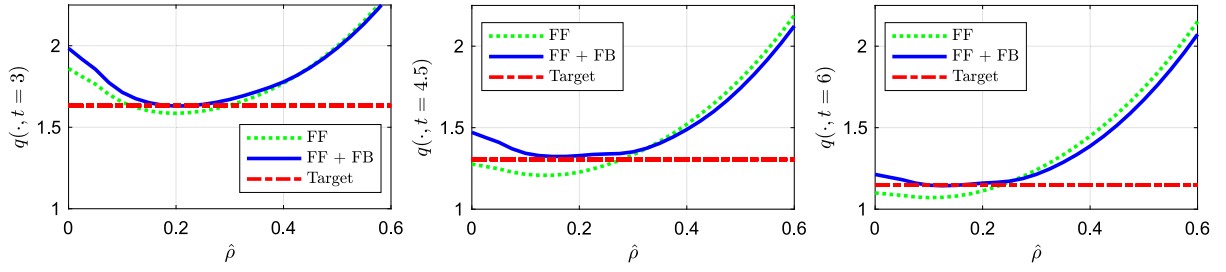
Fig. 14. Case 1 - moving ECCD: safety factor profile - $t = 3$ s (left), $t = 4.5$ s (center), $t = 6$ s (right).
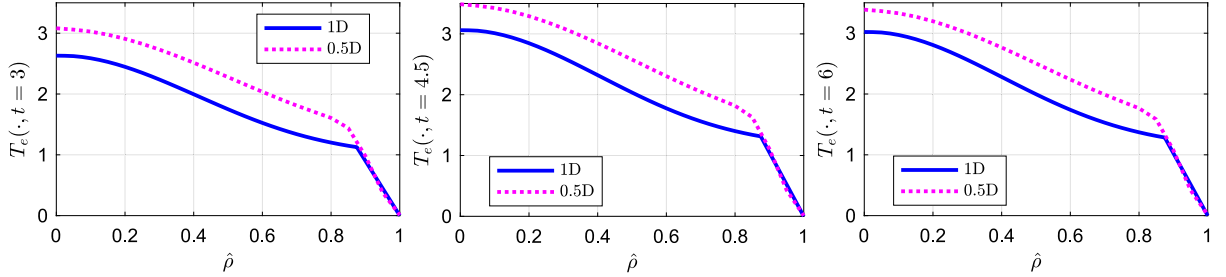
Fig. 15. Case 1 - moving ECCD: electron temperature profile as predicted by the simulator (1D) and synthesis (0.5D) models - $t = 3$ s (left), $t = 4.5$ s (center), $t = 6$ s (right).
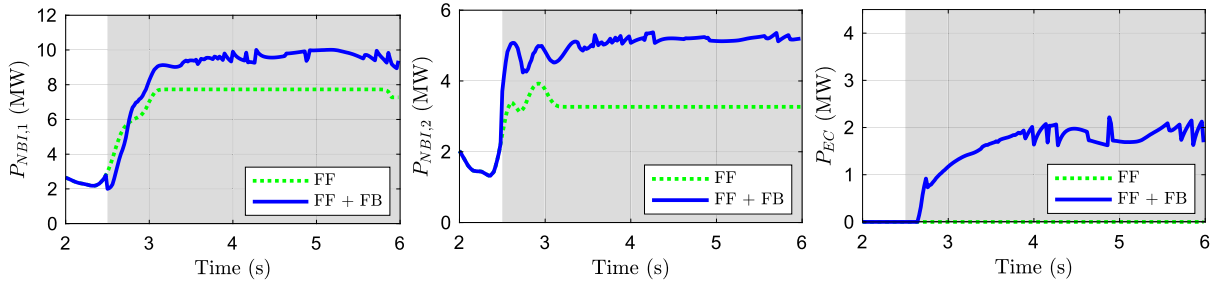
Fig. 16. Case 1 - moving ECCD: auxiliary powers - $P_{NBI,1}$ (left), $P_{NBI,2}$ (center), P_{EC} (right).
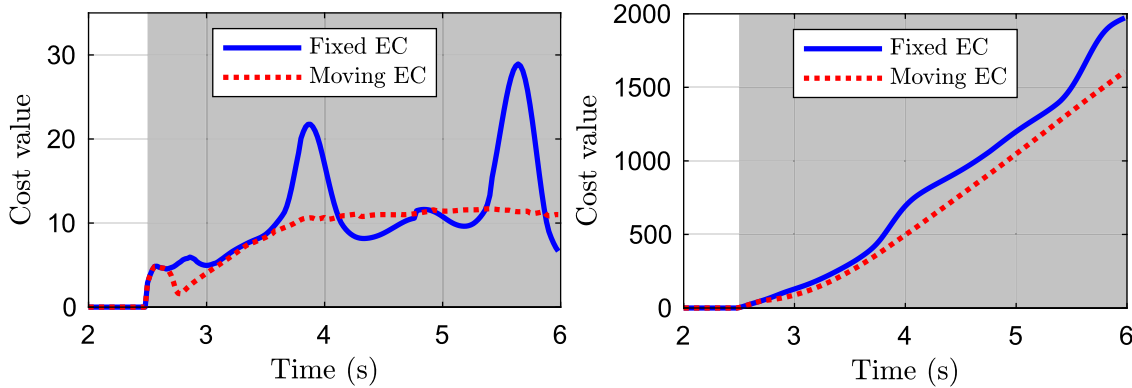
Fig. 17. Case 1 - instantaneous (left) and cumulative (right) cost values.

in Fig. 21. The effect of the overshoot caused by the W controller on the q_{min} controller can be seen in the auxiliary inputs shown in Fig. 22. Unlike the results presented in Section 4.1, it is clear that there is no saturation and spikes in the auxiliary inputs (excluding the initial spike) even when the ECCD is fixed.

The results corresponding to the moving ECCD simulations of Case 2 are presented in Figs. 23, 24, 25, 26 and 27. Fig. 23 presents the feedforward only and the feedforward+feedback W evolution. The corresponding P_{tot} values determined by the controller are also presented in the figure. The minimum safety factor and the optimal ECCD

position, as determined by the controller, are shown in Fig. 24. The open and closed-loop safety-factor profiles are shown in Fig. 25. The corresponding inputs are shown in Fig. 27. The figure shows that the optimal ECCD position slowly converges towards the minimum safety factor's location. The controller's performance is similar to that of the fixed ECCD case. One noticeable difference is in the initial spike in the auxiliary powers when the controller is activated, which are not as significant as those in the fixed ECCD case.

The discrepancy in the 1D simulator and 0.5D synthesis electron-temperature profiles shown in Figs. 21 and 26 appears as q_{min} model
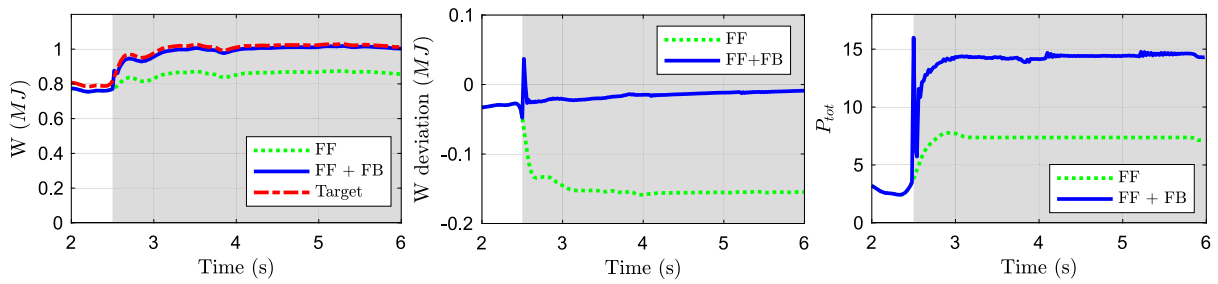
Fig. 18. Case 2 - fixed ECCD: W (left), $\tilde{W}$ (center), P_{tot} (right).
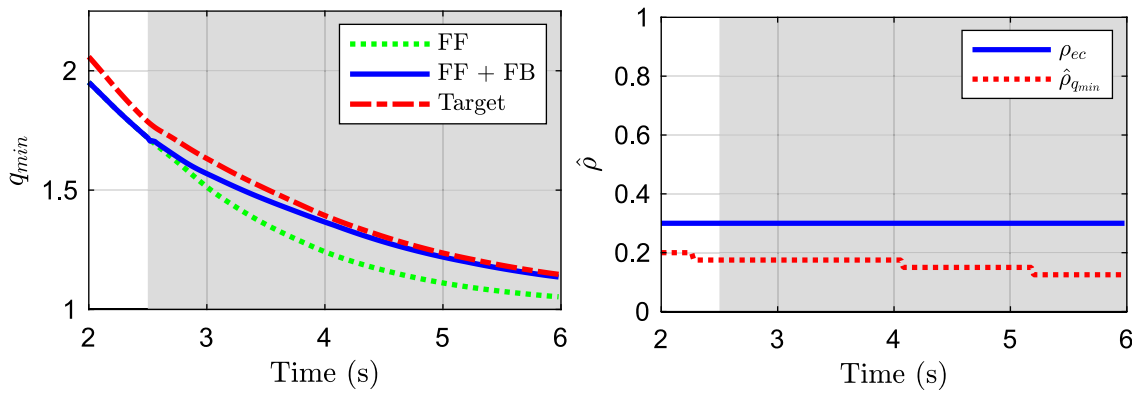
Fig. 19. Case 2 - fixed ECCD: q_{min} evolution (left), ECCD position (right).
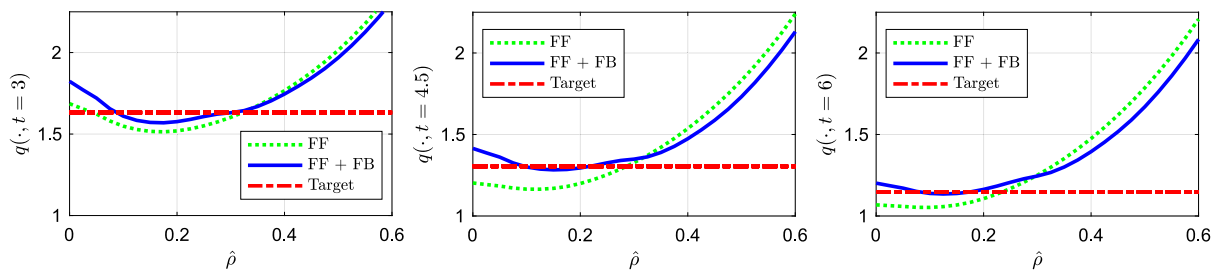
Fig. 20. Case 2 - fixed ECCD: safety factor profile - $t = 3$ s (left), $t = 4.5$ s (center), $t = 6$ s (right).
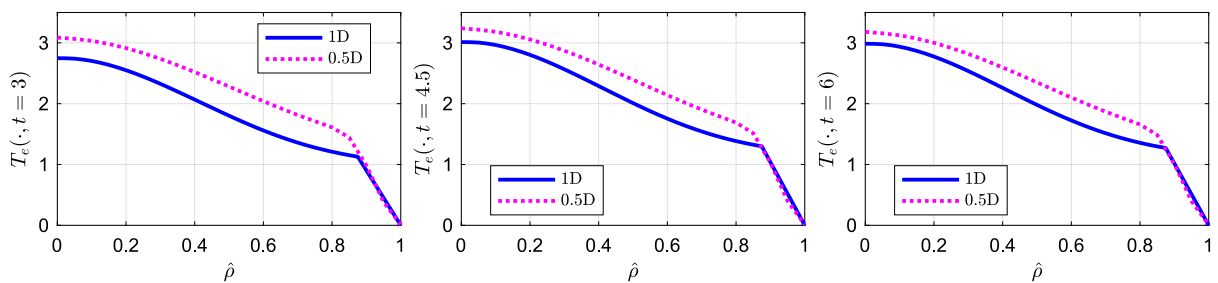
Fig. 21. Case 2 - fixed ECCD: electron temperature profile as predicted by the simulator (1D) and synthesis (0.5D) models - $t = 3$ s (left), $t = 4.5$ s (center), $t = 6$ s (right).
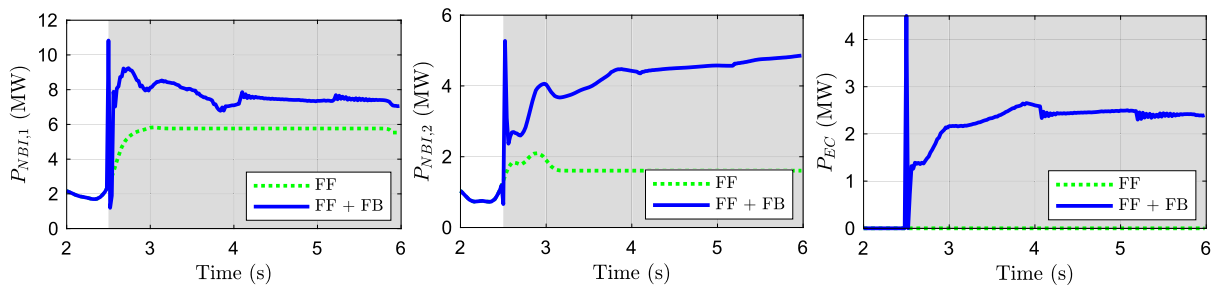
Fig. 22. Case 2 - fixed ECCD: Auxiliary powers - $P_{NBI,1}$ (left), $P_{NBI,2}$ (center), P_{EC} (right).
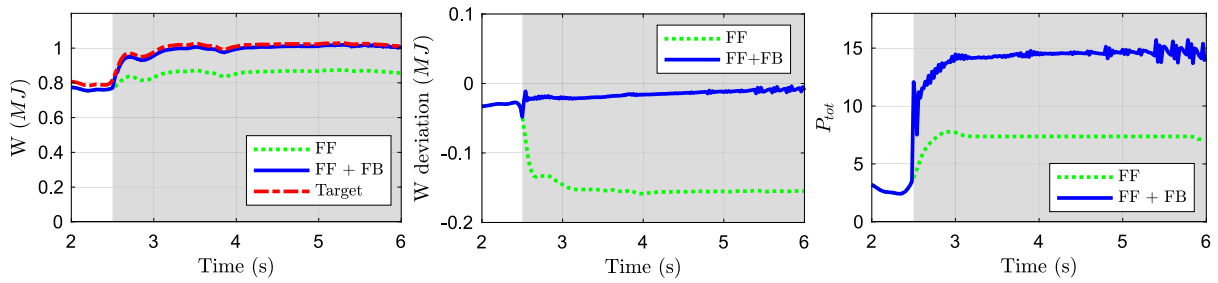
Fig. 23. Case 2 - moving ECCD: W (left), $\tilde{W}$ (center), P_{tot} (right).
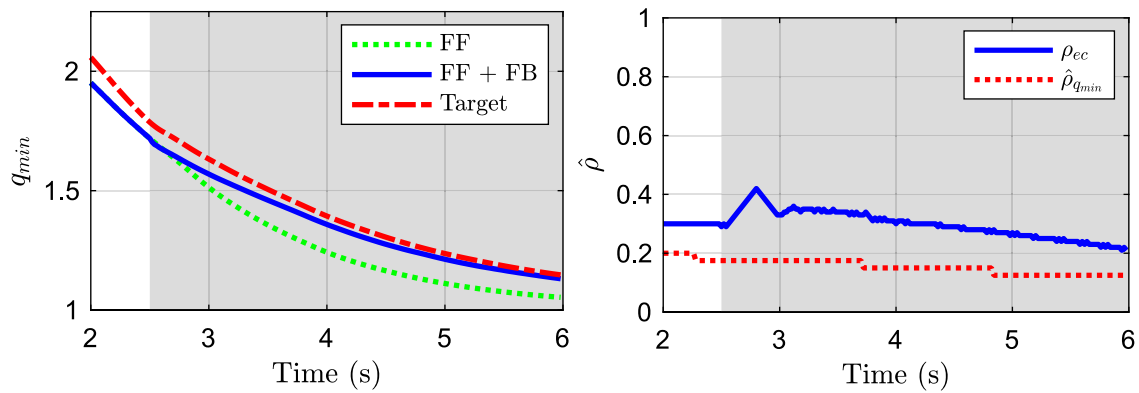
Fig. 24. Case 2 - moving ECCD: q_{min} evolution (left), ECCD position (right).
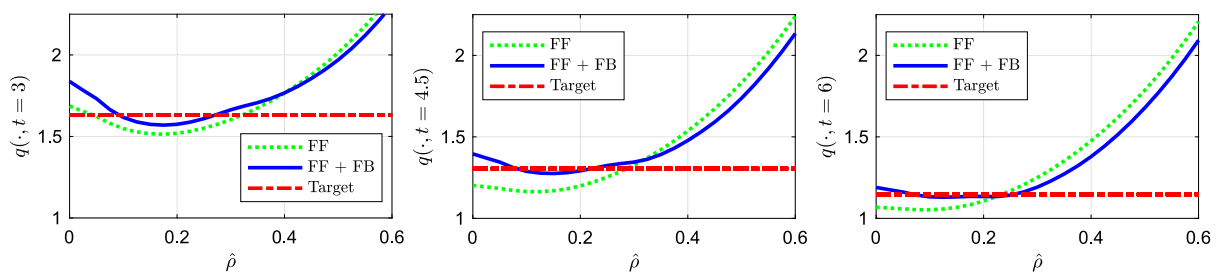
Fig. 25. Case 2 - moving ECCD: safety factor profile - $t = 3$ s (left), $t = 4.5$ s (center), $t = 6$ s (right).
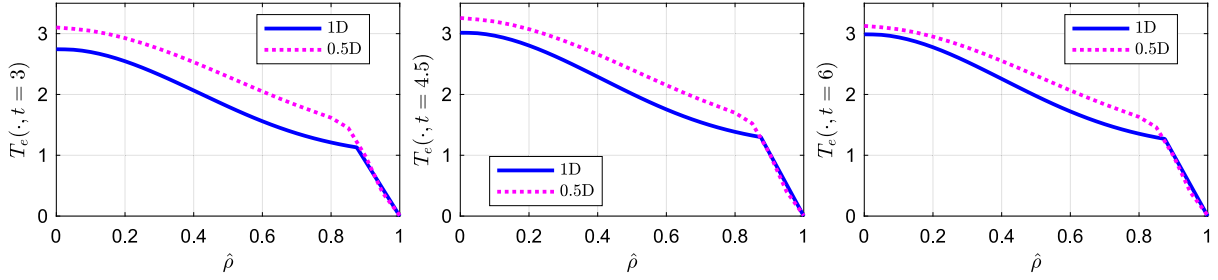
Fig. 26. Case 2 - moving ECCD: electron temperature profile as predicted by the simulator (1D) and synthesis (0.5D) models - $t = 3$ s (left), $t = 4.5$ s (center), $t = 6$ s (right).
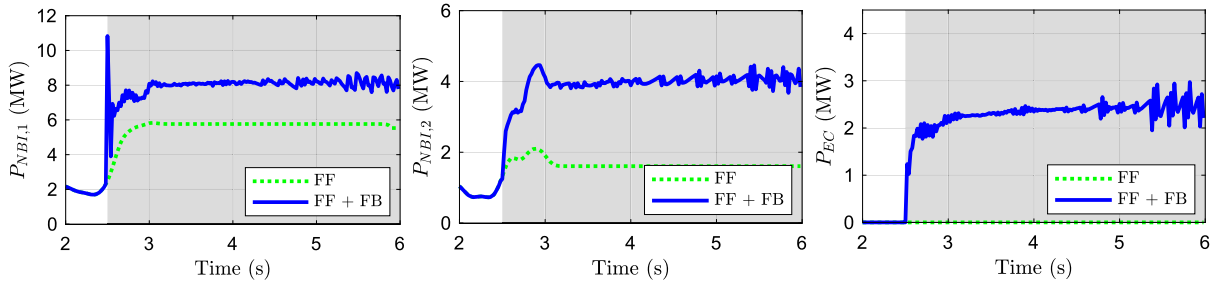
Fig. 27. Case 2 - moving ECCD: auxiliary powers - $P_{NBI,1}$ (left), $P_{NBI,2}$ (center), P_{EC} (right).
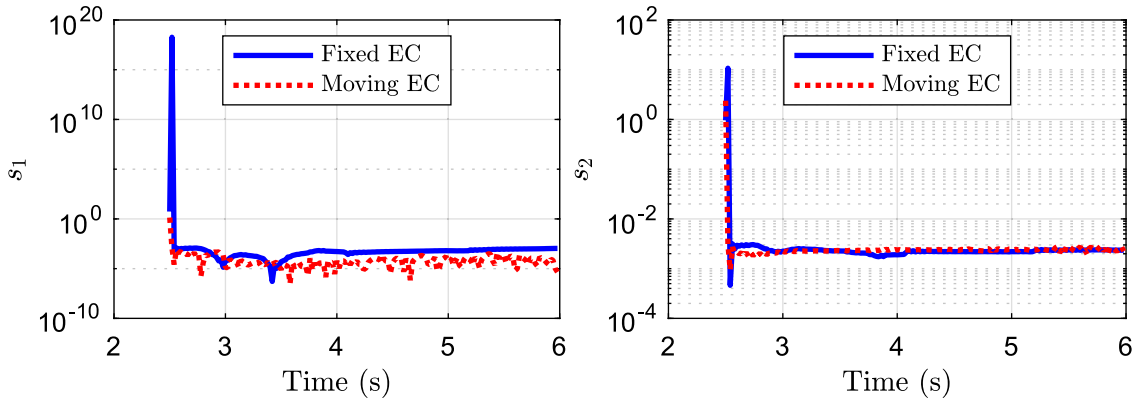
Fig. 28. Case 2 - fixed and moving ECCD slack variables comparison.

uncertainty. However, the integral action in the controller is able to handle the effect of uncertainty on the closed-loop performance.

One way to compare the performance of the controllers when the ECCD is fixed and moving is to consider the slack variables. Recall that the slack variables are included in the optimization problem to ensure the existence of a solution. However, large values of the slack variables imply that the optimization constraints, defined by (36) and (37), are not satisfied. Fig. 28 presents the slack variables for both the fixed and moving ECCD cases. The figure illustrates that the slack variables of the fixed ECCD case illustrate a more significant spike when the controller is turned on at 2.5 s. This spike in slack variables for the fixed ECCD case is also reflected in the auxiliary powers and the deviation of the total energy from the target in Figs. 22 and 18, respectively. In contrast, the corresponding figures for the moving ECCD case (Figs. 27 and 23) exhibit no or minimal spikes. Thus, optimally varying the

ECCD position could improve performance, even when the fixed ECCD controller ultimately meets the overall control objective.

5. Conclusion

A novel approach to model the evolution of the minimum safety factor is presented. The control-oriented model is a non-autonomous ordinary differential equation that continuously tracks the system dynamics at the minimum safety factor's location. Furthermore, the developed model incorporates the effect of the ECCD position on the system dynamics. Such a model enables the development of controllers that treat ECCD position as one of the controllable variables. Another primary contribution of this work is the development of an integrated total energy and minimum safety factor controller with a moving ECCD. The proposed nonlinear control algorithms are based on feedback linearization of the nonlinear models. A robust version of the minimum

safety factor controller is also discussed. A computationally inexpensive algorithm is developed to make the proposed controller viable for practical implementation. Numerical simulations in COTSIM are used to assess the effectiveness of the proposed controller for a DIII-D tokamak scenario. Simulation results demonstrate that using a moving ECCD can avoid the saturation of certain non-inductive powers and/or a high spike in actuator powers. Future extensions of this work can include experimental validation of the proposed controller and development of control algorithms for different profile control problems.

CRediT authorship contribution statement

Sai Tej Paruchuri: Writing – original draft, Visualization, Validation, Software, Methodology, Investigation, Formal analysis, Conceptualization. **Andres Pajares:** Software, Formal analysis, Conceptualization. **Tariq Rafiq:** Writing – review & editing, Supervision. **Eugenio Schuster:** Writing – review & editing, Supervision, Project administration, Funding acquisition.

Declaration of competing interest

The authors declare that they have no known competing financial interests or personal relationships that could have appeared to influence the work reported in this paper.

Data availability

The authors do not have permission to share data.

Acknowledgments

Disclaimer

This report was prepared as an account of work sponsored by an agency of the United States Government. Neither the United States Government nor any agency thereof, nor any of their employees, makes any warranty, express or implied, or assumes any legal liability or responsibility for the accuracy, completeness, or usefulness of any information, apparatus, product, or process disclosed, or represents that its use would not infringe privately owned rights. Reference herein to any specific commercial product, process, or service by trade name, trademark, manufacturer, or otherwise does not necessarily constitute or imply its endorsement, recommendation, or favoring by the United States Government or any agency thereof. The views and opinions of authors expressed herein do not necessarily state or reflect those of the United States Government or any agency thereof.

Appendix A. Poloidal flux gradient evolution

Incorporating the 0.5D models for the electron temperature (10) and electron density (9) into (5) and (6) results in

$$\eta = \hat{g}_\eta u_\eta, \tag{A.1}$$

$$j_{ni} = \sum_{i=1}^{N_{NBI}} \hat{g}_{NBI,i}\hat{u}_{NBI,i} + \hat{g}_{EC}\hat{u}_{EC} + \hat{g}_{BS}\left(\frac{\partial\psi}{\partial\hat{\rho}}\right)^{-1}\hat{u}_{BS}, \tag{A.2}$$

where

$$\hat{g}_\eta = Z_{eff}k_{sp}\left(T_e^{prof}\left(n_e^{prof}\right)^\zeta\right)^{-3/2},$$

$$\hat{g}_{NBI,i} = j_{NBI,i}^{prof}\left(T_e^{prof}\right)^{\epsilon_{NBI}}\left(n_e^{prof}\right)^{(\zeta\epsilon_{NBI}-1)},$$

$$\hat{g}_{EC} = j_{EC}^{prof}\left(T_e^{prof}\right)^{\epsilon_{EC}}\left(n_e^{prof}\right)^{(\zeta\epsilon_{EC}-1)},$$

$$\hat{g}_{BS} = \frac{R_0}{\hat{F}}\left[2\mathcal{L}_{31}T_e^{prof}(n_e^{prof})^\zeta(n_e^{prof})'\right.$$
$$\left. + \left(2\mathcal{L}_{31} + \mathcal{L}_{32} + \alpha\mathcal{L}_{34}\right)n_e^{prof}\left(T_e^{prof}(n_e^{prof})^\zeta\right)'\right],$$

$$u_\eta = \left(I_p^\gamma P_{tot}^\epsilon \bar{n}_e^\zeta\right)^{-3/2},$$

$$\hat{u}_{NBI,i} = (I_p^\gamma P_{tot}^\epsilon \bar{n}_e^\zeta)^{\epsilon_{NBI}}\bar{n}_e^{-1}P_{NBI,i},$$

$$\hat{u}_{EC} = (I_p^\gamma P_{tot}^\epsilon \bar{n}_e^\zeta)^{\epsilon_{EC}}\bar{n}_e^{-1}P_{EC},$$

$$\hat{u}_{BS} = \left(I_p^\gamma P_{tot}^\epsilon \bar{n}_e^\zeta\right)\bar{n}_e.$$

Substituting the above equations into the magnetic diffusion Eq. (3) results in a partial differential equation (PDE) of the form

$$\dot{\psi} = (g_{\eta,1}\theta' + g_{\eta,2}\theta)u_\eta + \sum_{i=1}^{N_{NBI}} g_{NBI,i}u_{NBI,i}$$
$$+ g_{EC}u_{EC} + g_{BS}\frac{1}{\theta}u_{BS}, \tag{A.3}$$

where $\theta := \frac{\partial\psi}{\partial\hat{\rho}}$, and $(\cdot)$, $(\cdot)'$ represents the temporal and spatial derivatives. The spatial terms in the above PDE are given by

$$g_{\eta,1} = \frac{\hat{g}_\eta D_\psi}{\mu_0\rho_b^2\hat{F}^2}, \qquad g_{\eta,2} = \frac{\hat{g}_\eta\left(\hat{\rho}D_\psi\right)'}{\mu_0\rho_b^2\hat{F}^2\hat{\rho}}, \tag{A.4}$$

$$g_{NBI,i} = \hat{g}_\eta R_0\hat{H}\hat{g}_{NBI,i}, \qquad g_{EC} = \hat{g}_\eta R_0\hat{H}\hat{g}_{EC}, \tag{A.5}$$

$$g_{BS} = \hat{g}_\eta R_0\hat{H}\hat{g}_{BS}, \tag{A.6}$$

and the virtual inputs terms are given by

$$u_{NBI,i} = u_\eta\hat{u}_{NBI,i}, \qquad u_{EC} = u_\eta\hat{u}_{EC}, \tag{A.7}$$

$$u_{BS} = u_\eta\hat{u}_{BS}. \tag{A.8}$$

Taking the partial derivative on both sides of (A.3) with respect to the spatial variable $\hat{\rho}$ gives

$$\dot{\theta} = \left(h_{\eta,1}\theta'' + h_{\eta,2}\theta' + h_{\eta,3}\theta\right)u_\eta + \sum_{i=1}^{N_{NBI}} h_{NBI,i}u_{NBI,i}$$
$$+ h_{EC}u_{EC} + \left(h_{BS,1}\frac{1}{\theta} - h_{BS,2}\frac{\theta'}{\theta^2}\right)u_{BS}, \tag{A.9}$$

where $h_{\eta,1} = g_{\eta,1}$, $h_{\eta,2} = (g_{\eta,1})' + g_{\eta,2}$, $h_{\eta,3} = (g_{\eta,2})'$, $h_{NBI,i} = (g_{NBI,i})'$, $h_{EC} = (g_{EC})'$, $h_{BS,1} = (g_{BS})'$ and $h_{BS,2} = g_{BS}$.

Appendix B. Stability analysis of the proposed controller

The asymptotic stability of the closed-loop system (34) is shown in this section using Lyapunov analysis. Before proceeding to the analysis, it is important to understand some of the basic definitions. Consider a nonlinear system governed by the ordinary differential equation

$$\dot{x} = f(x), \tag{B.1}$$

where $x \in \mathbb{R}^n$ is the state and $f : \mathbb{R}^n \mapsto \mathbb{R}^n$ is a known nonlinear function. A point $x_e \in \mathbb{R}^n$ is said to be an equilibrium of the above system is $f(x_e) = 0$. In other words, the system does not exhibit any dynamics when it is at an equilibrium. The nature of equilibrium is characterized by the system's behavior when the state x is "close" to x_e. For instance, an equilibrium x_e is said to be stable if for any arbitrary $\epsilon > 0$, there exists a $\delta > 0$ such that if the initial condition t_0 is such that $\|x(t_0) - x_e\| < \delta$, then for all $t > 0$, $\|x(t) - x_e\| < \epsilon$. The equilibrium is said to asymptotically stable if the equilibrium is stable and there exists a $\delta > 0$ such that $\lim_{t\to\infty}\|x - x_e\| = 0$. If δ is arbitrarily large, then the equilibrium is said to be globally asymptotically stable.

Lyapunov theory provides a necessary condition for the stability of a nonlinear system's equilibrium. According to the Lyapunov theorem, is there exists a positive definite continuously differentiable function $V : x \mapsto V(x) \in \mathbb{R}$ such that its time derivative $\dot{V}$ is negative definite, then the equilibrium x_e is asymptotically stable [34]. This theorem is

used in the following analysis to show that the controller tracks a given target minimum safety factor.

Consider the Lyapunov function

$$V = \frac{1}{2} x^T \underbrace{\begin{bmatrix} 1 & b \\ b & K_I \end{bmatrix}}_{P} x, \tag{B.2}$$

where $x = [x_1, x_2]^T = [\tilde{\theta}_{q_{min}}, \int_{t_0}^{t} \tilde{\theta}_{q_{min}} dt]^T$ is the augmented state vector, and $0 < b < \min(\sqrt{K_I}, K_P K_I / (K_I + \frac{1}{4} K_P^2))$. By definition, the above function is continuously differentiable. Furthermore, by choosing the constant b such that $0 << \sqrt{K_I}$, the eigenvalues of the matrix P in (B.2) will be positive, which in turn implies that the above function is positive definite. The time derivative of this Lyapunov function is

$$\dot{V} = -(K_P - b)x_1^2 - K_I b x_2^2 - K_p b x_1 x_2 \tag{B.3}$$

is negative definite. The global asymptotic stability of the error system is a direct consequence of the Lyapunov theorem [34]. This implies $\lim_{t \to \infty} \|x\| \to 0$, which implies $\tilde{\theta}_{q_{min}} \to 0$.

Even though the Lyapunov analysis implies global stability, the analysis is valid only for the closed-loop system. Recall that the closed-loop Eq. (34) is achieved through nonlinear cancellation, discussed in Section 3.3. From (32), it is clear that the value of nonlinearity to be canceled depends on the time derivative of the target $\dot{\theta}_{q_{min}}(t)$. The actuator saturation constrains the range of targets that the feedback linearizer can effectively cancel. This, in turn, implies that the controller may not drive the minimum safety factor to its target if actuators saturate and fail to cancel the nonlinearities.

Appendix C. Robust version of minimum safety factor controller

The control-oriented model developed in Section 2 does not account for model inaccuracies. To account for such uncertainties that arise in practical scenarios, an additive uncertainty term δ is introduced into the control-oriented model (25). The new control-oriented model takes the form

$$\dot{\theta}_{q_{min}}(t) = c_1(t) + c_2(t) + h(t)^T u_{ff}(t)$$
$$+ h(t)^T u_{fb}(t) - \dot{\theta}_{q_{min}}(t) + \delta. \tag{C.1}$$

The uncertainty term δ at any given instant is unknown. Thus, it is not possible to achieve nonlinearity cancellation as in (34). Suppose that the absolute value of the uncertainty term is bounded from above by a constant at all time t, i.e., $|\delta(t)| \leq \bar{\delta}$ for all t. To eliminate the effect of uncertainty on the controller performance, the robust control law given by

$$v = -K_p \tilde{\theta}_{q_{min}} - K_I \int_{t_0}^{t} \tilde{\theta}_{q_{min}} dt$$
$$- \bar{\delta} sign \left(\tilde{\theta}_{q_{min}} + b \int_{t_0}^{t} \tilde{\theta}_{q_{min}} dt \right). \tag{C.2}$$

is used instead of (33). In the above robust control law, the term b is defined as in the Lyapunov analysis in Appendix B. Using the new control law results in the closed loop system of the form

$$\dot{\tilde{\theta}}_{q_{min}} = -K_p \tilde{\theta}_{q_{min}} - K_I \int_{t_0}^{t} \tilde{\theta}_{q_{min}} dt$$
$$- \bar{\delta} sign \left(\tilde{\theta}_{q_{min}} + b \int_{t_0}^{t} \tilde{\theta}_{q_{min}} dt \right) + \delta. \tag{C.3}$$

Using the Lyapunov analysis similar to the one in Appendix B, one can show that the equilibrium $\tilde{\theta} = 0$ of the system governed by (C.1) is asymptotically stable.

Appendix D. Optimization analysis using Lagrange multiplier theorem

The optimization problem discussed in Section 3.4.1 is defined as the minimization of a quadratic cost function subject to two linear constraints. The Lagrange multiplier theorem is used in this section to derive a closed-form equation for the solution of the simplified optimization problem. Define $g_1^* := g_1(\hat{\rho}_{ec}, \cdot)$, $\hat{h}^* := \hat{h}(\hat{\rho}_{ec})$ and $h^* := h(\hat{\rho}_{ec})$. Now, define the Lagrangian as

$$\mathcal{L}(u, \lambda_1, \lambda_2) = f(u) - \lambda_1 g_1^*(u) - \lambda_2 g_2(u), \tag{D.1}$$

where $\lambda_1, \lambda_2 \in \mathbb{R}$ are the Lagrange multipliers. The Lagrange multiplier theorem [35] states that if a local minimum u^* exists, and the Jacobian $\begin{bmatrix} \nabla_u g_1^*(u^*) & \nabla_u g_2^*(u^*) \end{bmatrix}^T$ has maximal rank (which is 2 in this case), then there exist λ_1^* and λ_2^* such that

$$\nabla \mathcal{L}(u^*, \lambda_1^*, \lambda_2^*) = 0, \tag{D.2}$$

where ∇ represents the gradient. The above condition is equivalent to

$$\nabla_u f(u^*) - \lambda_1^* \nabla_u g_1^*(u^*) - \lambda_2^* \nabla_u g_2(u^*) = 0, \tag{D.3}$$

$$g_1^*(u^*) = 0, \tag{D.4}$$

$$g_2(u^*) = 0, \tag{D.5}$$

where the gradient vector

$$\nabla_u := \begin{bmatrix} \frac{\partial}{\partial u_1} & \cdots & \frac{\partial}{\partial u_{N_{NBI}+1}} & \frac{\partial}{\partial s_1} & \frac{\partial}{\partial s_2} \end{bmatrix}^T. \tag{D.6}$$

It is known that $\nabla_u f(u^*) = Q u^*$, $\nabla_u g_1^*(u^*) = \hat{h}^*$, and $\nabla_u g_2(u^*) = \hat{\mathbb{1}}$. Substituting these terms into (D.3) yields

$$u^* = \frac{1}{2} Q^{-1} \left(\lambda_1^* \hat{h}^* + \lambda_2^* \hat{\mathbb{1}} \right). \tag{D.7}$$

Substituting the expression for u^* into (D.4) and (D.5) gives us

$$\underbrace{\begin{bmatrix} \hat{h}^{*T} Q^{-1} \hat{h}^* & \hat{h}^{*T} Q^{-1} \hat{\mathbb{1}} \\ \hat{\mathbb{1}}^T Q^{-1} \hat{h}^* & \hat{\mathbb{1}} Q^{-1} \hat{\mathbb{1}} \end{bmatrix}}_{\mathbb{A}} \underbrace{\begin{Bmatrix} \lambda_1^* \\ \lambda_2^* \end{Bmatrix}}_{\Lambda} = \underbrace{\begin{bmatrix} -2b_1 \\ -2b_2 \end{bmatrix}}_{b}. \tag{D.8}$$

Thus, the closed form solution of the optimal inputs u^* is given by

$$u^* = \frac{1}{2} Q^{-1} \begin{bmatrix} \hat{h}^* & \hat{\mathbb{1}} \end{bmatrix} \mathbb{A}^{-1} b. \tag{D.9}$$

The Lagrange multiplier theorem gives a necessary condition for the local minimum of the cost function. For the simplified optimization problem, the extremum u^* indeed corresponds to the minimum of the cost function. This can be understood by considering level sets $f(u) = p$ of the cost function, where p is some arbitrary positive constant. By definition, these level sets form concentric ellipses. Furthermore, the points that satisfy both linear constraints ($g_1^* = 0$ and $g_2 = 0$) form a hyperplane. The extremum u^*, defined by (D.9), corresponds to the point at which the level set with the least cost (or equivalently the smallest value of p) is tangential to the hyperplane.

Appendix E. Control algorithm for computing feedback inputs with saturation limits

The following algorithm gives computationally efficient approach to compute the feedback control inputs that satisfy the saturation limits. In essence, the algorithm first solves the optimization problem without the constraint given in (38). If any of the input values are outside the saturation limits, the algorithm sets their values equal to the limits and minimizes the cost function corresponding to the rest of the actuators. Note that the ECCD center is still fixed at $\hat{\rho}_{ec} \in [0, 1]$ in the above algorithm.

Algorithm 1: Algorithm for computing the saturated inputs for a given ECCD position.

Inputs: h^*, b_1, b_2, Q.
Outputs: u^*.

1. Set $\tilde{h} = [\ ]$, an empty vector; and calculate u^* using (D.9).
2. For $i = 1, \ldots, N_{NBI} + 1$,

   - if $u_i <= \underline{\gamma}_i$
     $$b_1 = b_1 + \underline{\gamma}_i * h_i^*, \qquad b_2 = b_2 + \underline{\gamma}_i$$
   - elseif $u_i >= \bar{\gamma}_i$
     $$b_1 = b_1 + \bar{\gamma}_i * h_i^*, \qquad b_2 = b_2 + \bar{\gamma}_i$$
   - else
     $$\tilde{h} = [\tilde{h}; h_i^*], \qquad \tilde{q} = [\tilde{q}; q_i]$$

3. Set $h^* = \tilde{h}$, $\mathbb{1} = ones(size(\tilde{h}))$,
   $Q = diag(\tilde{q}, q_{s_1}, q_{s_2})$.
4. If $size(h^*) == 0$
      stop,
   else
      return to Step 1.

Appendix F. Control algorithm for computing feedback inputs and optimal ECCD position

The algorithm given below uses an iterative approach to compute the optimal ECCD position and the corresponding feedback control inputs that satisfy the constraints (36), (37), (38) and (39). At a given time step k, the algorithm first considers the set of possible ECCD positions Ω^k. For instance, if ρ_{ec}^{k-1} is the ECCD position at time step $k-1$ and δ is the maximum distance the ECCD position can change in the next time step, then one can define Ω^k as $\Omega^k := \left[\rho_{ec}^{k-1} - \delta, \rho_{ec}^{k-1}, \rho_{ec}^{k-1} + \delta\right]$. When δ is large, more intermediate points in the set Ω^k can be considered. The algorithm now computes the feedback auxiliary powers using Algorithm 1 for each ECCD position and choose the values corresponding to the least cost. Since the computations corresponding to each ECCD position are independent of each other, the optimal inputs $u^{*,k}$ at time step k corresponding to each ECCD position can be computed simultaneously through parallel computations. As a result, the algorithm given below is computationally inexpensive.

Algorithm 2: Algorithm for optimization problem with moving ECCD.
Inputs: ρ_{ec}^{k-1}.
Outputs: $u^{*,k}, \rho_{ec}^{*,k}$.

1. Define the vector
$$\Omega^k := \begin{cases} [0, \delta] & \text{if } \rho_{ec}^{k-1} = 0, \\ [1 - \delta, 1] & \text{if } \rho_{ec}^{k-1} = 1, \\ [\rho_{ec}^{k-1} - \delta, \rho_{ec}^{k-1}, \rho_{ec}^{k-1} + \delta] & \text{otherwise.} \end{cases}$$

   In the above definition, the term ρ_{ec}^{k-1} represents the position of the ECCD at the previous time step.

2. For $i = 1, \ldots,$ length of Ω^k,

   (a) Set $\hat{\rho}_{ec}^k = \Omega_i^k$.
   (b) Compute inputs $u_i^{*,k}$ with $\hat{\rho}_{ec}^k$ using Algorithm 1. Set $J_i^k = u_i^{*,k^T} Q u_i^{*,k}$.

3. Set j such that $J_j^k = min_i J_i^k$. Set $u^{*,k} = u_j^{*,k}$ and $\rho_{ec}^{*,k} = \Omega_j^k$.

References

[1] J. Wesson, D.J. Campbell, Tokamaks, vol. 149, Oxford University Press, 2011.

[2] A. Pajares, E. Schuster, Safety factor profile control in tokamaks via feedback linearization, in: 2016 IEEE 55th Conference on Decision and Control (CDC), 2016, pp. 5668–5673, http://dx.doi.org/10.1109/CDC.2016.7799140.

[3] M.D. Boyer, J. Barton, E. Schuster, T.C. Luce, J.R. Ferron, M.L. Walker, D.A. Humphreys, B.G. Penaflor, R.D. Johnson, First-principles-driven model-based current profile control for the DIII-D tokamak via LQI optimal control, Plasma Phys. Control. Fusion 55 (10) (2013) 105007, http://dx.doi.org/10.1088/0741-3335/55/10/105007.

[4] J.E. Barton, K. Besseghir, J. Lister, E. Schuster, Physics-based control-oriented modeling and robust feedback control of the plasma safety factor profile and stored energy dynamics in ITER, Plasma Phys. Control. Fusion 57 (11) (2015) 115003, http://dx.doi.org/10.1088/0741-3335/57/11/115003.

[5] M. Boyer, R. Andre, D. Gates, S. Gerhardt, I. Goumiri, J. Menard, Central safety factor and β_N control on NSTX-U via beam power and plasma boundary shape modification, using TRANSP for closed loop simulations, Nucl. Fusion 55 (5) (2015) 053033, http://dx.doi.org/10.1088/0029-5515/55/5/053033.

[6] A. Pajares, E. Schuster, Central safety factor control in DIII-D using neutral beam injection and electron cyclotron launchers in zero input-torque scenarios, in: 2017 IEEE Conference on Control Technology and Applications (CCTA), 2017, pp. 1460–1465, http://dx.doi.org/10.1109/CCTA.2017.8062664.

[7] W. Wehner, M. Lauret, E. Schuster, J.R. Ferron, C. Holcomb, T.C. Luce, D.A. Humphreys, M.L. Walker, B.G. Penaflor, R.D. Johnson, Predictive control of the tokamak q profile to facilitate reproducibility of high-q_{min} steady-state scenarios at DIII-D, in: 2016 IEEE Conference on Control Applications (CCA), Vol. 19, pp. 629–634, http://dx.doi.org/10.1109/CCA.2016.7587900.

[8] F. Imbeaux, M. Lennholm, A. Ekedahl, P. Pastor, T. Aniel, S. Brémond, J. Decker, P. Devynck, R. Dumont, G. Giruzzi, P. Maget, D. Mazon, A. Merle, D. Molina, P. Moreau, F. Saint-Laurent, J. Ségui, D. Zarzoso, Tore Supra Team, Real-time control of the safety factor profile diagnosed by magneto-hydrodynamic activity on the Tore Supra Tokamak, Nucl. Fusion 51 (7) (2011) 073033, http://dx.doi.org/10.1088/0029-5515/51/7/073033.

[9] T. Suzuki, S. Ide, T. Oikawa, T. Fujita, M. Ishikawa, M. Seki, G. Matsunaga, T. Hatae, O. Naito, K. Hamamatsu, M. Sueoka, H. Hosoyama, M. Nakazato, the JT-60 Team, Off-axis current drive and real-time control of current profile in JT-60U, Nucl. Fusion 48 (4) (2008) 045002, http://dx.doi.org/10.1088/0029-5515/48/4/045002.

[10] J. Ferron, P. Gohil, C. Greenfield, J. Lohr, T. Luce, M. Makowski, D. Mazon, M. Murakami, C. Petty, P. Politzer, M. Wade, Feedback control of the safety factor profile evolution during formation of an advanced Tokamak discharge, Nucl. Fusion 46 (10) (2006) L13, http://dx.doi.org/10.1088/0029-5515/46/10/L01.

[11] D. Moreau, D. Mazon, M. Ariola, G. De Tommasi, L. Laborde, F. Piccolo, F. Sartori, T. Tala, L. Zabeo, A. Boboc, E. Bouvier, M. Brix, J. Brzozowski, C. Challis, V. Cocilovo, V. Cordoliani, F. Crisanti, E. De La Luna, R. Felton, N. Hawkes, R. King, X. Litaudon, T. Loarer, J. Mailloux, M. Mayoral, I. Nunes, E. Surrey, O. Zimmerman, A two-time-scale dynamic-model approach for magnetic and kinetic profile control in advanced tokamak scenarios on JET, Nucl. Fusion 48 (10) (2008) 106001, http://dx.doi.org/10.1088/0029-5515/48/10/106001.

[12] C. Xu, Y. Ou, E. Schuster, Sequential linear quadratic control of bilinear parabolic PDEs based on POD model reduction, Automatica 47 (2) (2011) 418–426, http://dx.doi.org/10.1016/j.automatica.2010.11.001.

[13] W. Wehner, J. Barton, M. Lauret, E. Schuster, J.R. Ferron, C. Holcomb, T.C. Luce, D.A. Humphreys, M.L. Walker, B.G. Penaflor, R.D. Johnson, Optimal current profile control for enhanced repeatability of L-mode and H-mode discharges in DIII-D, Fusion Eng. Des. 123 (2017) 513–517, http://dx.doi.org/10.1016/j.fusengdes.2017.03.022.

[14] Y. Ou, C. Xu, E. Schuster, J. Ferron, T. Luce, M. Walker, D. Humphreys, Receding-horizon optimal control of the current profile evolution during the ramp-up phase of a tokamak discharge, Control Eng. Pract. 19 (1) (2011) 22–31, http://dx.doi.org/10.1016/j.conengprac.2010.08.006.

[15] E. Maljaars, F. Felici, T. Blanken, C. Galperti, O. Sauter, M. de Baar, F. Carpanese, T. Goodman, D. Kim, S. Kim, M. Kong, B. Mavkov, A. Merle, J. Moret, R. Nouailletas, M. Scheffer, A. Teplukhina, N. Vu, Profile control simulations and experiments on TCV: A controller test environment and results using a model-based predictive controller, Nucl. Fusion 57 (12) (2017) 126063, http://dx.doi.org/10.1088/1741-4326/aa8c48.

[16] E. Maljaars, F. Felici, M. de Baar, J. van Dongen, G. Hogeweij, P. Geelen, M. Steinbuch, Control of the tokamak safety factor profile with time-varying constraints using MPC, Nucl. Fusion 55 (2) (2015) 023001, http://dx.doi.org/10.1088/0029-5515/55/2/023001.

[17] F.B. Argomedo, E. Witrant, C. Prieur, S. Brémond, R. Nouailletas, J.-F. Artaud, Lyapunov-based distributed control of the safety-factor profile in a tokamak plasma, Nucl. Fusion 53 (3) (2013) 033005, http://dx.doi.org/10.1088/0029-5515/53/3/033005.

[18] F.B. Argomedo, E. Witrant, C. Prieur, D. Georges, S. Brémond, Model-based control of the magnetic flux profile in a Tokamak plasma, in: 49th IEEE Conference on Decision and Control (CDC), 2010, pp. 6926–6931, http://dx.doi.org/10.1109/CDC.2010.5717184.

["